

Strong coupling between a dielectric nanocavity and a monolayer transition metal dichalcogenide

F. Schröder,^{1,2} P. Wyborski,¹ M. Xiong,^{1,2} G. Kountouris,^{1,2} B. Munkhbat,¹
M. Wubs,^{1,2} P. T. Kristensen,^{1,2} J. Mørk,^{1,2} and N. Stenger^{1,2,*}

¹*Department of Electrical and Photonics Engineering,
Technical University of Denmark, Ørstedes Plads 343, 2800 Kgs. Lyngby, Denmark*

²*NanoPhoton - Center for Nanophotonics, Technical University of Denmark,
Ørstedes Plads 345A, 2800 Kgs. Lyngby, Denmark*

(Dated: June 25, 2025)

We demonstrate strong coupling between light in a dielectric nanocavity with deep sub-wavelength confinement and excitons in a monolayer of molybdenum ditelluride. Avoided crossing is demonstrated by both photoluminescence and reflection measurements, from which we extract a light-matter interaction strength of $g_{\text{PL}} = 5.3(3)$ meV and $g_{\text{R}} = 4.7(7)$ meV, respectively. The associated Rabi splitting is twice as large as the system's losses. These values are in good agreement with values obtained by a novel exciton reaction coordinate formalism, yielding $g_{\text{theory}} = 5.2(7)$ meV. The strong light-matter interaction, combined with low losses and sub-wavelength confinement of light, demonstrates a new regime of light-matter interactions where strong nonlinearities at the single-photon level are expected.

Monolayer (ML) transition-metal dichalcogenides (TMDCs), consisting of one molybdenum atom and two chalcogen atoms per unit cell, are direct bandgap semiconductors in the 2H phase [1, 2]. Their unique excitons, featuring high binding energy [3, 4], high absorption coefficient [5, 6], and large oscillator strength [7, 8], make them compelling platforms for exploring strong light-matter interactions [9]. Strong coupling occurs when the energy exchange between light and excitons is fast enough to surpass the system's decay rate, resulting in Rabi oscillations and hybridized polariton states [10–12]. The regime of strong light-matter interaction has been demonstrated with excitons in ML TMDCs coupled to optical microcavities, where light is confined on length scales similar to or larger than the wavelength of the light [13–18]. As these structures are based on dielectric materials, cavity-induced losses are small, and cavity linewidths are typically on the order of 0.1 meV to 10 meV. Other ways to achieve strong light-matter interactions with TMDCs and periodically-patterned dielectric structures are bound states in the continuum [19–21] and meta-surfaces [22, 23]. Similarly, TMDCs integrated with plasmonic structures, such as surface plasmon-polaritons [24, 25] and plasmonic nanocavities [26–29], can exhibit strong light-matter interactions. In the latter case, light is confined on deep sub-wavelength length scales, but the confinement is accompanied by significant metal-induced losses and plasmonic linewidths typically exceed 100 meV.

Integrating dielectric cavities, such as photonic crys-

tal cavities [30, 31] and nanobeam cavities [32] with ML molybdenum ditelluride (MoTe_2) is particularly promising due to its excitonic transition energy in the near-infrared [33]. This has led, for example, to weak coupling and enhanced spontaneous emission [34]. While recent advances have explored the light-matter interactions of ML TMDCs with dielectric nanobeam cavities [35, 36], strong coupling in these systems has not yet been achieved.

Recently, confinement of light on sub-wavelength scales using dielectric materials was realized [37–43]. Inverse design by topology-optimization has been demonstrated as a versatile tool for designing these cavities with extreme dielectric confinement (EDC) [44–46], and topology-optimized EDC cavities have been experimentally realized in silicon [42] and indium phosphide (InP) [43]. The sub-wavelength confinement, which was previously achievable only with plasmonic structures [47–49], comes without the associated ohmic and absorption losses intrinsic to plasmonic materials and therefore enables intriguing possibilities [50–53]. In particular, a recent study demonstrated lasing from a quantum well embedded in such an EDC cavity [54].

Similarly, the integration of EDC cavities with excitons in monolayer TMDCs unlocks new possibilities for exciton dynamics and device applications. Exciton-polaritons confined by a cavity mode to a single, sub-wavelength-scale region have been shown to exhibit strong exciton-exciton interactions [57–59]. The combination of near-plasmonic sub-wavelength confinement, low-loss dielectric

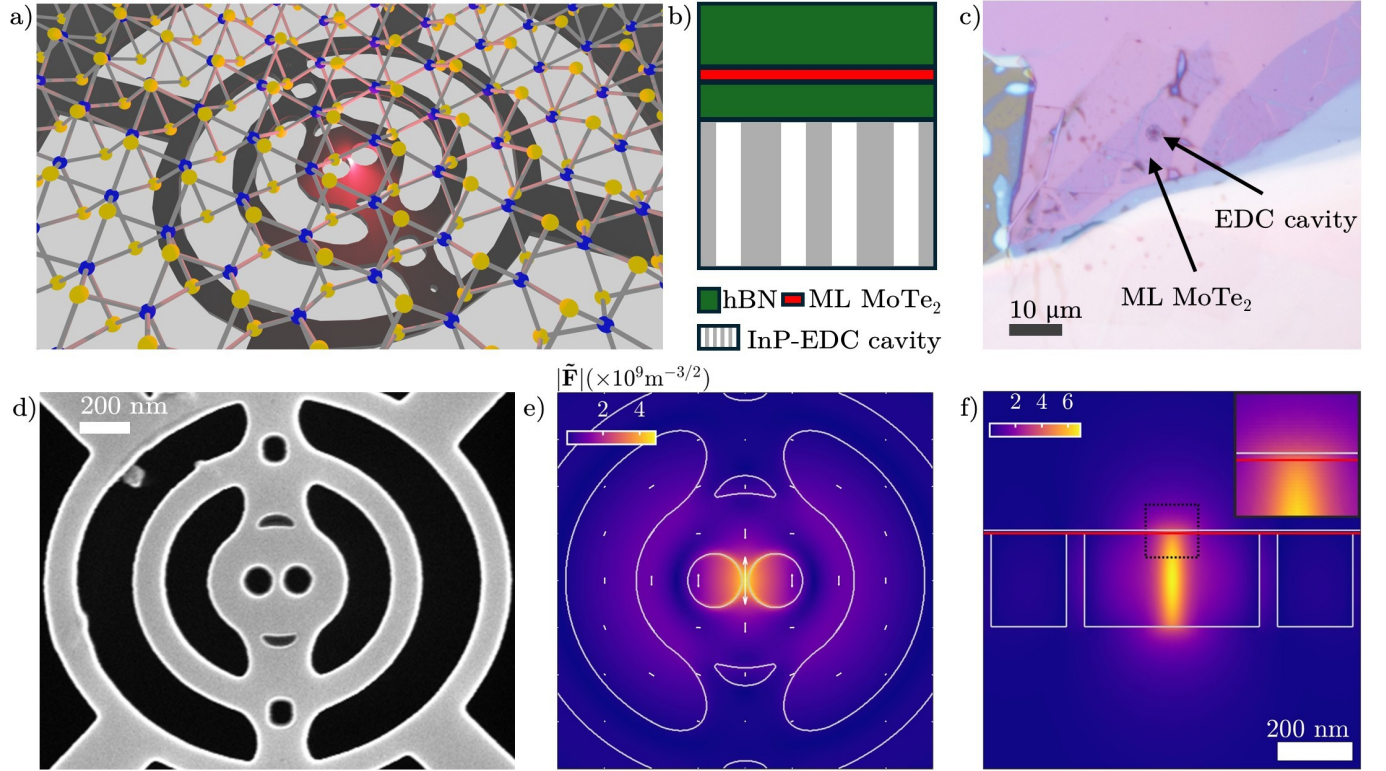


Figure 1. a) Artistic representation of the system. Light is confined in an EDC cavity [55, 56]. The ML MoTe₂ lies on top of the EDC cavity [55, 56]. The hBN flakes are not depicted. b) Sketch of the side view of the structure. c) Microscope image of the hBN-encapsulated ML MoTe₂ on the EDC cavity. d) SEM image of the passive cavity. e) Simulated electric-field distribution of the structure in e) the xy -plane at $z = z_{2D}$ and f) the yz -plane at $x = 0$. Contour lines show the topography of the cavity and the hBN layer. Arrows in (e) depict the in-plane polarization of the electric-field. The red line in (f) depicts the ML MoTe₂.

cavities, and the strong oscillator strength of excitons in monolayer TMDCs enables a novel regime for exploring strong light-matter interactions. Studying polaritons in this regime is of significant interest, as a nonlinearity in an interacting system yields photon antibunching [60, 61]. In particular, recent theoretical work [62] has shown that enhanced quantum nonlinearities at the single-photon level could be achieved, enabling a polariton blockade [62–64].

Moreover, the spin-valley selection rules of ML TMDCs support the study of chiral light-matter interactions [65–68], while the system also serves as a promising platform for exploring condensation effects [50]. Unlike plasmonic nanostructures, dielectric cavities integrate seamlessly with existing technology [41, 52, 69, 70], offering significant scalability and application benefits.

In this work, we experimentally demonstrate strong coupling between an InP-based EDC cavity with sub-wavelength confinement and excitons in ML MoTe₂. The

avoided crossing of the system is demonstrated with temperature-resolved photoluminescence (PL) and reflection measurements, in which the excitonic transition and the cavity mode are resonant at $T = 40$ K. The extracted light-matter interaction strength is approximately 5 meV. The extracted cavity linewidth is 3.3(1) meV, more than an order of magnitude smaller than typical plasmonic linewidths, while a lateral field confinement length of $\sigma \approx 70$ nm is maintained, more than a factor of two smaller than $\lambda/(2n)$. The obtained Rabi-splitting is twice as large as the losses of the system, and the experimentally obtained value is in agreement with numerical simulations based on the reaction-coordinate formalism [59]. This marks an important step towards the observation of exciton-exciton interactions and single-photon nonlinearities [62] in integrable photonic devices operating close to the O-band.

An artistic representation of the ML MoTe₂ on an EDC

cavity is depicted in Fig. 1(a). ML MoTe₂ is sandwiched in hexagonal Boron Nitride (hBN) to prevent degradation of the monolayer [71] and to reduce the linewidth [34, 72–74]. The resulting hBN/MoTe₂/hBN heterostructure is placed on the EDC cavity, cf. Fig. 1(b). The MoTe₂ layer is separated by 1.5(13) nm from the surface of the structured InP, and we refer to the z position of the ML MoTe₂ as z_{2D} . Please see Sec. in the Supplementary Information for details on the 2D material fabrication process. A microscope image of the resulting sample is depicted in Fig. 1(c). Due to the large extent of the ML MoTe₂ compared to the cavity mode, the excitons are considered delocalized in the plane but strictly confined in the z -direction [59]. Nevertheless, the exciton-polaritons are laterally confined due to interaction with the sub-wavelength cavity mode.

The EDC cavity design results from a simplified version of a topology-optimized (TO) structure, where the TO structure is approximated by only ellipses and tangents. This smoothes the topography while maintaining the overall structure of the original TO design, which has been shown to successfully retain the properties of the cavity [75]. A scanning electron microscope (SEM) image of a similar cavity on the same chip can be found in Fig. 1(d). The outer rings of the cavity increase the Q factor by suppressing radiative losses, similar to circular Bragg reflectors, while the holes in the center provide extreme dielectric confinement on sub-wavelength scales. The confinement is largely determined by the spacing of the void regions in the cavity center. A void spacing of 20 nm was targeted, safely above what has been determined as a fabrication limitation [43] while yielding a sub-wavelength field confinement (see below). The previous design targeted a resonance in the Telecom-C band. To acquire a design where the cavity resonance energy matches the excitonic transition of the A-exciton in ML MoTe₂ at cryogenic temperatures, the design was therefore scaled appropriately. The EDC cavity is fabricated in a 245 nm thick InP membrane [43]. This material system is chosen because the excitonic transition in MoTe₂ is below the bandgap of InP. Therefore, the system is not limited by absorption losses of the dielectric material.

The dominant response of the optical nanocavity can be accurately described by a single quasinormal mode (QNM) [76–81] with complex eigenenergy of the form $\tilde{E}_{\text{cav}} = E_{\text{cav}} - i\Gamma_{\text{cav}}/2$, in which E_{cav} denotes center position and Γ_{cav} is the full width at half maximum (FWHM) of the emission spectrum in the single-mode approximation. From numerical calculations, as detailed in the Supplementary Information, we find that the structure sup-

ports a QNM with nominal resonance energy of $E_{\text{cav}} = 1.187$ eV, a nominal quality Q factor of $Q = 571(7)$, and an effective mode volume of $V_{\text{eff}} = 0.060(2)(\lambda/n)^3$. We note, however, that dielectric nanocavities often exhibit significantly lower Q factors than predicted by simulations [42, 43], and we extract an experimental Q factor of 358(11) (see Sec. in the Supplementary Information). This reduction is primarily attributed to fabrication imperfections, such as surface roughness and geometric deviations [82]. Owing to their extreme field confinement, EDC cavities exhibit pronounced sensitivity to such imperfections [43]. Moreover, the resonance frequency is highly sensitive to small variations of the geometry [75]. Fig. 1(e) and (f) show the magnitude of the normalized field profile $|\tilde{\mathbf{F}}(\mathbf{r})|$ in the xy plane at z_{2D} and in the yz plane at $x = 0$, respectively. The arrows in Fig. 1(e) depict $\text{Re}[F_{x,y}(\mathbf{r})]$, highlighting the linear polarization of the cavity \tilde{E}_{cav} along the y axis [75, 83]. The lateral confinement length of the field in the MoTe₂ plane is estimated as $\sigma \approx 70$ nm (see Sec. in the Supplementary Information). The structure also supports another mode with orthogonal polarization, lower resonance energy, and reduced quality factor—rigorously analyzed in Ref. [83] and referred to as the low- Q mode.

For excitons in ML TMDCs coupled to dielectric nanocavities, the light-matter interaction strength g can be calculated using the QNMs in combination with material-specific properties of the ML TMDC [59, 84]. In this study, we follow Ref. [59] and describe the light-matter interaction in a reaction-coordinate formalism, in which g_{theory} can be expressed as

$$g_{\text{theory}} = \sqrt{\frac{\hbar^2 e_0^2}{\pi \epsilon_0 m_0^2 E_{\text{cav}} a_B^2} \sum_{\alpha} \int d^2 \mathbf{r} \left| \tilde{\mathbf{F}}(\mathbf{r}_{xy}, z_{2D}) \cdot \mathbf{p}_{\text{cv}}^{\alpha} \right|^2}, \quad (1)$$

where $\mathbf{p}_{\text{cv}}^{\alpha}$ denotes the transition dipole moment of the ML TMDC, α denotes the valley index K, K' [65], and a_B denotes the excitonic Bohr radius of the A-exciton. The relevant material parameters are extracted from Refs. [33, 85–90]. The integral is performed in the xy plane of the ML MoTe₂, cf. Fig. 1(e), as indicated with the red line in Fig. 1(f). From Eq. 1 it follows that the light-matter interaction strength strongly depends on the polarization of the cavity mode. If we consider a linearly-polarized cavity mode with $\tilde{\mathbf{F}}(\mathbf{r}_{xy}, z_0) = F_0(\mathbf{r}_{xy}, z_0) \hat{e}_y$, then g reaches its maximal value of $\mathbf{p}_{\text{cv}}^{\alpha} \parallel \hat{e}_y$ and vanishes for $\mathbf{p}_{\text{cv}}^{\alpha} \perp \hat{e}_y$. Eq. 1 is solved numerically, yielding $g_{\text{theory}} = 5.2(7)$ meV, see Sec. in the Supplementary Information for details on the numerical calculations.

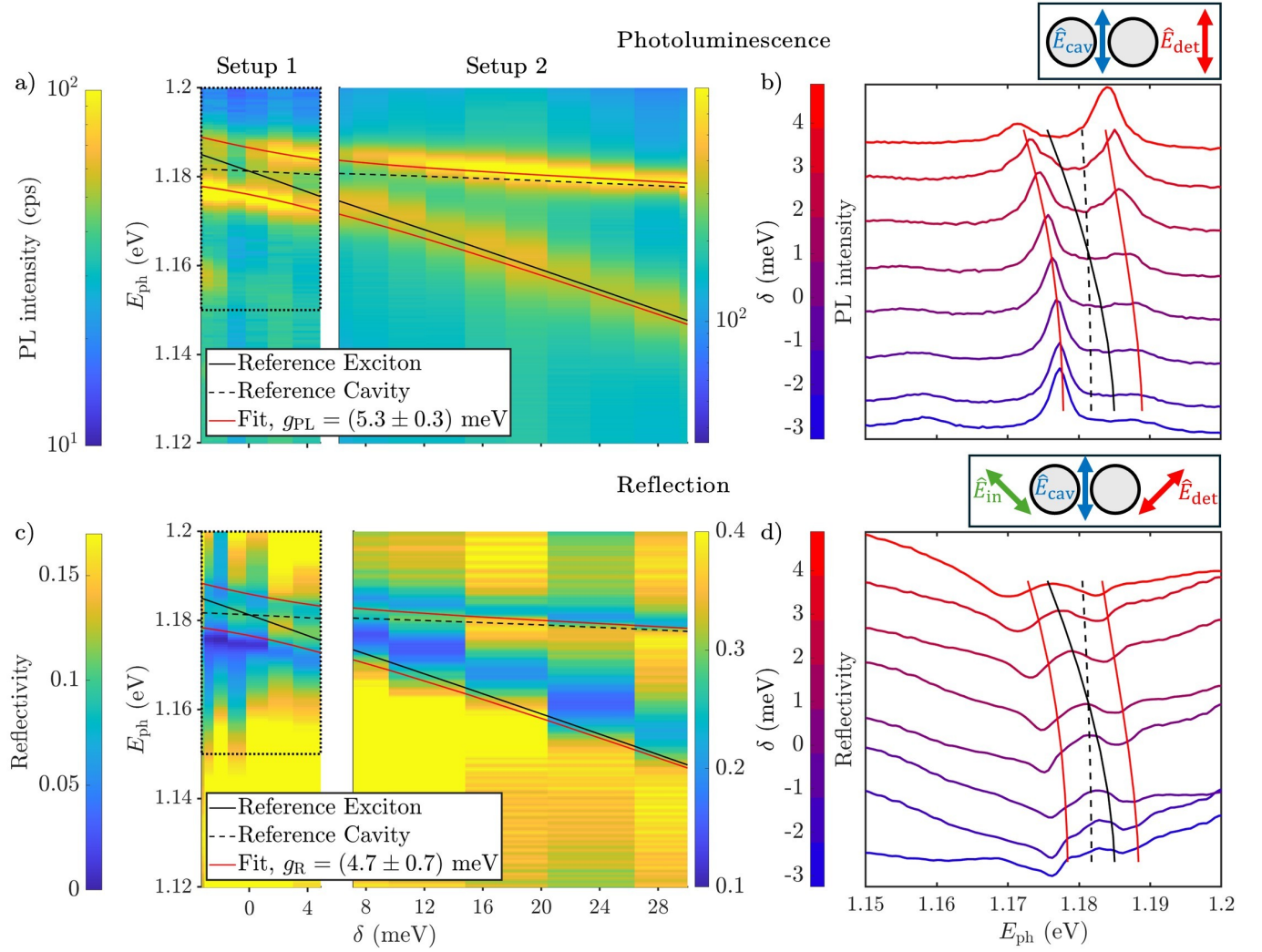


Figure 2. a) and b) PL spectra as a function of detuning, recorded with the detection polarization aligned with the cavity mode. The dotted box in (a) depicts the region of the spectra depicted in (b). The solid and dashed black line depicts the reference for the exciton and for the cavity mode, respectively, see Sec. in the Supplementary Information. c) and d) Reflectivity spectra recorded in a cross-polarization configuration. Setups 1 and 2 are explained in the main text.

We investigate PL spectra as a function of temperature T with the detection polarization \hat{E}_{det} oriented parallel to \hat{E}_{cav} . Temperature variations primarily affect the excitonic emission energy E_{exc} through the bandgap temperature dependence and modify the exciton linewidth Γ_{exc} due to phonon interactions. At $T = 4$ K, we extract $\Gamma_{exc} = 5.1(9)$ meV, in good agreement with Ref. [91]. In contrast, the cavity resonance energy E_{cav} is influenced by the temperature dependence of the refractive index, but its variation is much smaller than the changes in E_{exc} . The cavity linewidth is determined as $\Gamma_{cav} = 3.3(1)$ meV.

We explore these dependencies systematically in order to calculate the detuning $\delta = E_{cav} - E_{exc}$, see Sec. in the Supplementary Information for details. Fig. 2(a) shows the PL as a function of detuning in a range from $T = 4$ K to $T = 163$ K. In addition, Fig. 2(b) shows the associated line plots in a region of interest close to zero detuning, as indicated in panel (a). In both panels (a) and (b), fits from reference measurements of the uncoupled cavity and of the uncoupled excitons are shown as black dashed and solid lines, respectively. We go from negative detuning to positive values in the measured temperature range, with

$T = 40$ K corresponding to $\delta = -0.2(7)$ meV. Clearly, avoided crossing is observed, which is a hallmark of strong light-matter coupling.

We use two different setups for different temperature regimes as indicated in Fig. 2(a), see Appendix for details. Setup 1 contains a liquid-helium cryostat for $T \leq 70$ K, corresponding to $\delta \leq 4.9(7)$ meV. Setup 2 contains a liquid-nitrogen cryostat for $T \geq 79$ K, corresponding to $\delta \geq 6.2(10)$ meV. A small spectral offset is often observed when comparing data acquired with different setups due to imperfect alignment and calibration of the spectrometers. We carefully compare the reference measurements acquired with both setups (cf. Sec. in the Supplementary Information) and deduce an offset of approximately 3 meV between the data from Setups 1 and 2; see Fig. A1 in the Appendix. The data from Setup 2 in Fig. 2(a) and (c) have been corrected accordingly. We note that Setup 1 provides a range from $\delta = -3.3(7)$ meV to $\delta = 4.9(7)$ meV, and therefore the data from Setup 1 alone already provide evidence of avoided crossing. To assess the light-matter interaction strength, we fit the extracted peak positions of the lower (E_-) and of the upper (E_+) polariton with the real part of a coupled-oscillator model, see Sec. and in the Supplementary Information for details. The fit result, indicated as the red lines in Fig. 2(a) and (b), yields $g_{\text{PL}} = 5.3(3)$ meV. This value is on the same order as obtained for a ML TMDC on a nanobeam cavity [35, 36], despite the much tighter light confinement in this work. This is in line with the prediction that the light-matter interaction strength is largely determined by the out-of-plane confinement [59] and not by the mode volume, as for example for quantum dots in microcavities [92]. However, as shown in Ref. [62], exciton-exciton interactions are largely determined by the lateral confinement, highlighting the potential of the reported results for future studies on nonlinearities.

The PL measurements are supplemented with reflection measurements in a cross-polarization configuration, see Appendix for details [83]. Fig. 2(b) and (c) depict reflection spectra as a function of δ . As observed from PL measurements, the avoided crossing is clearly visible as two dips in the reflection spectra, confirming hybridization of excitons and photons. A fit of the reflection measurements with the coupled-oscillator model yields $g_{\text{R}} = 4.7(7)$ meV, which agrees well with the value obtained from PL measurements. Notably, the experimentally obtained values g_{R} and g_{PL} are in excellent agreement with the value obtained with the exciton-reaction coordinate formalism $g_{\text{theory}} = 5.2(7)$ meV, as discussed above.

Strong coupling is usually identified when the number of oscillations in the polariton states N_{Rabi} exceeds one [93]. This is achieved when [10, 11, 28]

$$N_{\text{Rabi}} = \frac{2E_{\text{Rabi}}}{\Gamma_{\text{exc}} + \Gamma_{\text{cav}}} \geq 1 \Leftrightarrow E_{\text{Rabi}} \geq \frac{\Gamma_{\text{exc}} + \Gamma_{\text{cav}}}{2}, \quad (2)$$

with $E_{\text{Rabi}} = \sqrt{4g^2 - (\Gamma_{\text{cav}} - \Gamma_{\text{exc}})^2}/4$ denoting the Rabi splitting. To assess the Rabi splitting, the cavity and exciton linewidth are evaluated at $T = 40$ K/ $\delta = -0.2(7)$ meV, yielding $\Gamma_{\text{cav}} = 3.3(1)$ meV and $\Gamma_{\text{exc}} = 6.0(7)$ meV see Sec. in the Supplementary information for details. Together with the aforementioned values for g , we find $E_{\text{Rabi}} = 10.6(7)$ meV and $9.4(15)$ meV as deduced from PL and reflection measurements, respectively. This value agrees well with the energy splitting of the polaritonic emission determined from the peak positions at $\delta = -0.2(7)$ meV, $E_+ - E_- = 10.1(3)$ meV and $9.4(7)$ meV for PL and reflection measurements, respectively. As $E_{\text{Rabi}} > (\Gamma_{\text{exc}} + \Gamma_{\text{cav}})/2 = 4.7(4)$ meV, E_{Rabi} overcomes the averaged losses in the system by more than a factor of two. We deduce $N_{\text{Rabi}} = 2.3(1)$ and $2.0(2)$ for PL and reflection measurements, respectively, and we conclude that the system is clearly in the strong-coupling regime.

We note that in a coupled-oscillator model, the light-matter interaction strength is in general complex-valued [51, 84, 94]. To evaluate the magnitude of the complex part of the light-matter interaction strength, we fit the extracted peak positions and the linewidths, corresponding to the real and the imaginary parts of the eigenvalues, respectively, see Sec. in the Supplementary Information for details. We find that the coupled-oscillator model also fits the linewidths accurately, which is additional confirmation of the reported strong light-matter interaction. Moreover, we find that the imaginary part of the light-matter interaction strength is less than 6 % of the real part and is almost zero within the error bars.

Finally, we turn our attention to the polarization properties of the photoluminescence signal. As the cavity mode is linearly polarized, orienting the detection polarization parallel to the cavity mode polarization enables the study of the strongly coupled system. On the other hand, by orienting the detection polarization perpendicular to the cavity mode, primarily residual excitons, that do not couple to the cavity mode are detected. Those are excited in the ML MoTe₂ in the vicinity of the cavity mode. The emission is studied at $T = 50$ K, corresponding to $\delta = 1.4(7)$ meV. Fig. 3 show the PL spectra as a function of the angle of the halfwave ($\lambda/2$) plate $\theta_{\lambda/2}$

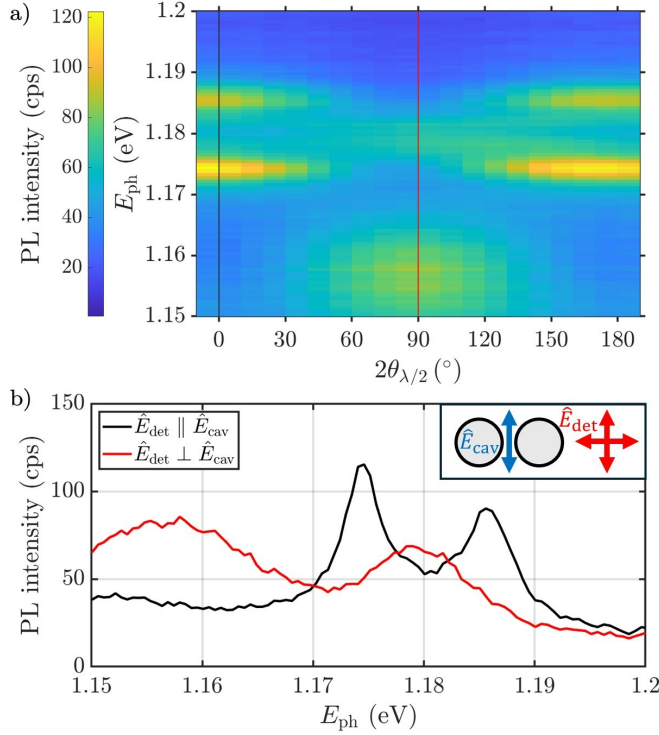


Figure 3. a) PL spectra at $T = 50$ K as a function of $\theta_{\lambda/2}$ in front of the analyzer. b) PL spectra from (a) with the analyzer oriented parallel and perpendicular to the cavity mode for black and red lines, respectively.

in front of the analyzer. Together with the analyzer, rotating the $\lambda/2$ plate by $\theta_{\lambda/2}$ effectively rotates the detection polarization state by twice that value. Two peaks, separated by 11 meV and associated with the polaritonic emission, are identified for $\hat{E}_{\text{cav}} \parallel \hat{E}_{\text{det}}$, corresponding to $2\theta_{\lambda/2} = 0^\circ$ and 180° , see Fig. 3. Choosing $2\theta_{\lambda/2} = 90^\circ$ yields a detection polarization perpendicular to the orientation of the cavity mode. One peak centered between the two polaritonic peaks is detected, corresponding to emission from residual excitons that do not couple to the cavity mode. Another peak is observed at $E_{\text{ph}} = 1.157$ eV for $\hat{E}_{\text{det}} \perp \hat{E}_{\text{cav}}$. This is well explained by another mode in the cavity. In Ref. [83], we demonstrate that in addition to the mode of interest in this work, the EDC cavity supports a mode with slightly lower eigenenergy, lower Q factor, and orthogonal polarization. The excitation of this low- Q mode could be due to trions, which are known to exist at a lower transition energy than excitons in the ML MoTe₂ [95].

In summary, we have demonstrated strong coupling be-

tween excitons in a ML MoTe₂ and light confined by an EDC cavity on sub-wavelength length scales. The light-matter interaction strength is deduced both from photoluminescence and reflection measurements, yielding $g_{\text{PL}} = 5.3(3)$ meV and $g_{\text{R}} = 4.7(7)$ meV. These values are consistent with our numerical calculation exploiting the exciton-reaction coordinate-formalism [59], for which we find the value $g_{\text{theory}} = 5.2(7)$ meV. Polarization-projection of the fluorescence signal confirms the polaritonic nature. This reported system serves as an ideal testbed for studying nanoscale confined light-matter interactions. It combines the small losses of dielectric nanocavities ($\Gamma_{\text{cav}} = 3.3(1)$ meV) and sub-wavelength lateral field confinement ($\sigma \approx 70$ nm $< \lambda/(2n)$). Hence, the polaritons are confined on sub-wavelength scales by both the out-of-plane confinement of the ML and the in-plane confinement of the dielectric nanocavity. The tight confinement is expected to facilitate strong nonlinearities [57, 58, 62], and combined with small losses, is expected to give rise to the polariton-blockade effect [60–63]. Moreover, it supports research on condensation effects [50] and chiral interactions [65, 67].

ACKNOWLEDGEMENTS

We thank Dorte R. Danielsen, Duc Hieu Nguyen, Philip Holm, and Manh-Ha Dohan for the fruitful discussion about 2D material fabrication, as well as Peter Bøggild and Timothy J. Booth for their support. This work was supported by the Danish National Research Foundation through NanoPhoton - Center for Nanophotonics, grant number DNRFF147. N. S. acknowledges funding by the Novo Nordisk Foundation NERD Programme (project QuDec NNF23OC0082957). P.W. and B.M. acknowledge support from the European Research Council (ERC-StG *TuneTMD*, grant no. 101076437), and the Vilum Foundation (grant no. VIL53033). P.W. and B.M. also acknowledge the European Research Council (ERC-CoG *Unity*, grant no. 865230) and Carlsberg Foundation (grant no. CF21-0496).

APPENDIX: EXPERIMENTAL SETUPS

Two setups are used to access the temperature regime from room temperature to 4 K. Setup 1 contains a closed-cycle liquid-helium cryostat (AttoDRY800XS, *Attocube*), giving us access to $T \leq 70$ K. Setup 2 contains a liquid-nitrogen cryostat (HFS600, *Linkam Scientific*), allowing

us to measure $T \geq 79$ K. In both setups, the system is excited with a red laser ($\lambda_{\text{laser}} = 650$ and 637.5 nm for Setups 1 and 2, respectively). The excitation light beam is directed via a dichroic mirror (Setup 1)/ a 50/50 beam-splitter (Setup 2) to a microscope objective, focusing the light on the sample. The emitted light is, after polarization projection with a $\lambda/2$ plate and a linear polarizer (= analyzer), detected by a spectrometer. A longpass filter ensures the filtering of the excitation light beam. We note that small deviations of the recorded wavelengths are likely to occur when comparing spectra recorded in both setups due to imperfect alignment of the spectrometers. Such an offset is evident in all measurements, see Sec. and Sec. . We extract the offset from the reference measurements (cf. Sec.). Fig. A1 shows the peak energy of the reference cavity as a function of temperature. The fit of the peak position with a parabola is indicated as the red lines. A shift in photon energy is observed between $T \leq 70$ K and $T \geq 79$ K, arising from the imperfect alignment of the respective spectrometers used in Setups 1 and 2. The $E_{\text{cav,ref}}(T)$ from Setup 1 and 2 is extrapolated to 75 K, and the offset is calculated as $E_{\text{cav,ref}}^{\text{Setup1}}(75 \text{ K}) - E_{\text{cav,ref}}^{\text{Setup2}}(75 \text{ K})$. This yields an offset of 3 meV (cf. Fig. A1), and the data from Setup 2 in Fig. 2 have been shifted accordingly.

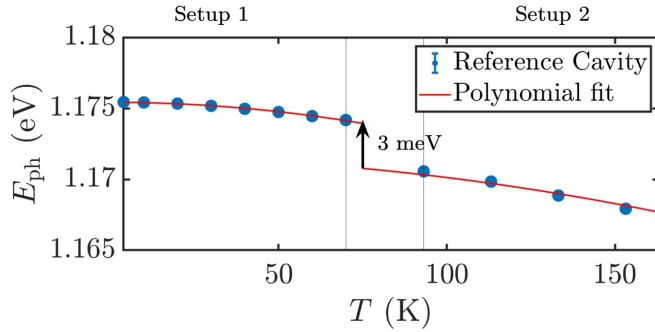


Figure A1. Extracted peak energy from the reference cavity as a function of temperature. The red lines denote a fit with a parabola. The temperature regions of Setup 1 and 2 are indicated. The deduced offset is marked by the black arrow.

Adaptions to our PL setups allow us to carry out reflection measurements. For that, we change the light source to a superluminescent diode (SLD1050P, *Thorlabs*). In addition to the analyzer and the $\lambda/2$ plate in the detection path, we insert a linear polarizer and a $\lambda/2$ plate in the excitation path, as well as a quarter-wave ($\lambda/4$) plate in the detection path. In Setup 1, the dichroic mirror is exchanged with a 50/50 beamsplitter.

The reflection measurements are carried out in a cross-polarization configuration, where the polarization of the incoming light \hat{E}_{in} is perpendicular to the detection polarization \hat{E}_{det} , for example $\hat{E}_{\text{in}} = \hat{x}$, $\hat{E}_{\text{det}} = \hat{y}$. The sample is oriented so that the linear polarization of the cavity mode is oriented 45° with respect to both of them, e.g. $\hat{E}_{\text{cav}} = \frac{1}{\sqrt{2}}(\hat{x} + \hat{y})$ [82, 83]. The quarter-wave plate is carefully adjusted to suppress elliptically polarized elements induced by scattering at the glass window of the cryostat. All spectra have been normalized with a reference spectrum recorded on a gold surface.

Supplementary Information: Strong coupling between a dielectric nanocavity and a monolayer transition metal dichalcogenide

2D material fabrication

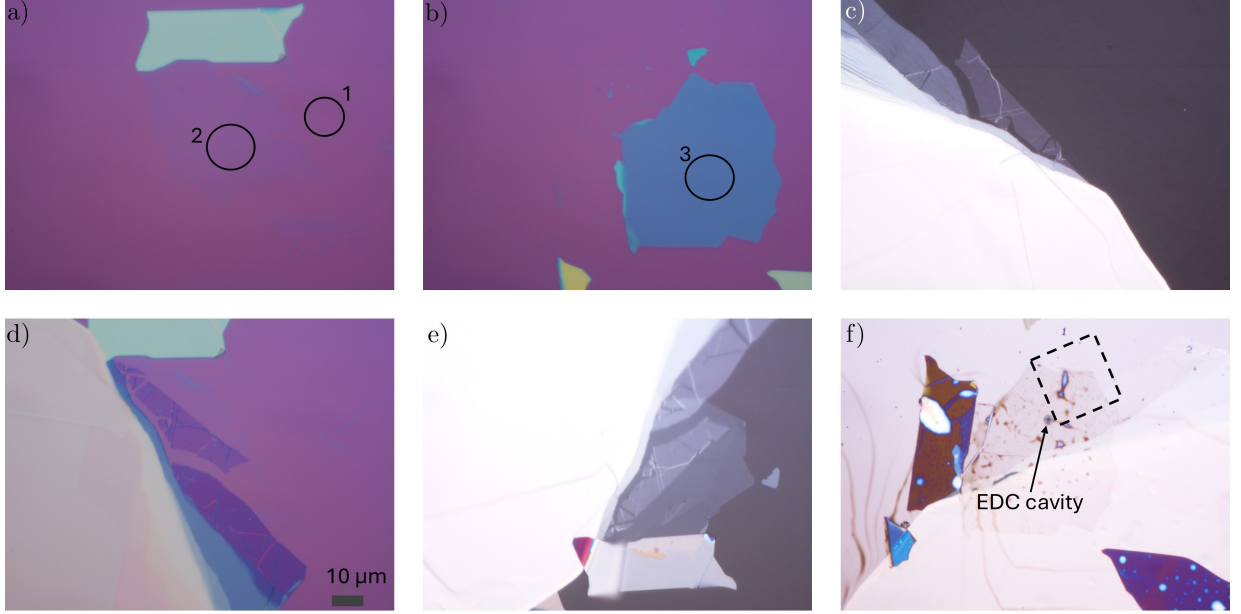


Figure S1. Microscope image with 100x magnification after each fabrication step. a) Lower hBN flake on a 300 nm SiO_2/Si substrate. The flake of interest is the faint purple region in the center of the image. b) Upper hBN flake on a 300 nm SiO_2/Si substrate. The circles in (a) and (b) indicate the regions where the RGB color values are extracted. c) MoTe_2 on a PDMS substrate. d) MoTe_2 on lower hBN on a 300 nm SiO_2/Si substrate. e) hBN/ MoTe_2 /hBN heterostructure on the PC/PDMS stamp. f) Heterostructure on the EDC cavity. The dashed rectangle in (f) indicates the region where the AFM map was taken, see Fig. S3.

In this Supplementary Information, the 2D material fabrication process is described. Firstly, MoTe_2 and hBN (*HQ Graphene*) are mechanically exfoliated on polydimethylsiloxane (PDMS) on a glass slide and on a 300 nm silicon dioxide (SiO_2) on a silicon (Si) wafer, respectively (cf. Fig. S1(a)-(c)). The flake depicted in Fig. S1(a) is labeled as the lower hBN flake, while the flake depicted in (b) is labeled as the upper hBN flake. The thicknesses of the hBN flakes are determined with the optical contrast method [96].

	Marker	R	G	B	t_R (nm)	t_G (nm)	t_B (nm)
Substrate	1	136	82	140	0	0	0
lower hBN flake	2	135	88	146	0	2.0	2.4
upper hBN	3	79	110	166	8.5	9.3	9.3

Table I. Extracted color values for red (R), green (G), and black (B) at markers 1-3 corresponding to the substrate, to the lower, and to the upper hBN flake. The deduced thicknesses from the RGB color values are denoted as t_R , t_G , and t_B for red, green, and black, respectively.

A calibration of the microscope was pursued in Ref. [97], and the color values for red (R), green (G), and black (B) from the optical images correspond to a certain thickness. The RGB color values for the substrate and for

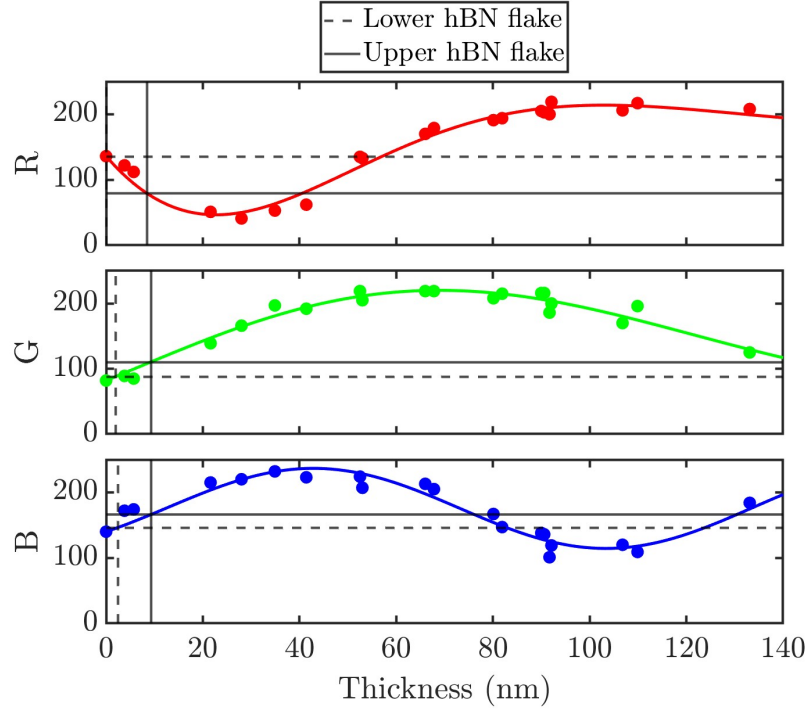


Figure S2. Calibration of the microscope images. RGB color values of hBN flakes as a function of thickness. Data points are from Ref. [97] except for the value of the substrate, cf. Tab. I. The grey dashed and solid lines mark the extracted values for the lower and the upper hBN flakes, respectively.

the flakes are determined; see markers 1-3 in Fig. S1(a)-(b). These are summarized in Tab. I. Fig. S2 depicts the calibration function for hBN flakes. The data points in Fig. S2 are from Ref. [97]. In addition, the value for the substrate (cf. Tab. I) is included. The colored solid lines depict a fit of the data points with the general fit function $V(t) = A_1 e^{-at} \sin(kt + \varphi) + A_2$, where V denotes either the R, G or B value, and t denotes thickness. The fit is constrained to match the substrate value, ensuring positive thicknesses. The RGB values read from Tab. I for the lower and upper hBN flakes are indicated as grey dashed and solid lines, respectively. With those values, the intersect with the fit curve yields the thicknesses t_R , t_G and t_B for R, G, and B, respectively (also indicated with grey dashed and solid lines). The determined thicknesses are summarized in Tab. I. The average of the three thicknesses is formed to determine the best estimate and the standard deviation for the thickness, yielding $t_{\text{hBN,lower}} = 1.5(13) \text{ nm}$ and $t_{\text{hBN,upper}} = 9.0(5) \text{ nm}$.

The 2D materials are stacked using a commercially available transfer system (*HQ Graphene*). The monolayer MoTe_2 is placed on the thin hBN flake with a dry-transfer method [98]. The lower hBN flake on the substrate is placed on a hot plate on a three-axis micrometer stage. Another three-axis micrometer stage holds the glass slide with the MoTe_2 flake. The lower hBN flake and the ML MoTe_2 are aligned with an optical microscope and pressed together. Then, the hotplate is heated up to 60°C to ensure that the ML sticks to the hBN flake, see Fig. S1(d). After that, the upper hBN flake is picked up with a polycarbonate (PC)/polydimethylsiloxane (PDMS) film [99, 100]. The stamp is pressed on the upper hBN flake at 60°C . The hotplate is set to 110°C when contact is established. After 5 minutes, the substrate is moved down, and the hBN flake sticks to the PC film. The hBN/ MoTe_2 heterostructure (HS) is picked up by the upper hBN flake on a PC/PDMS film, pressing them together at 110°C . After waiting for 5 minutes and moving the substrate down again, the hBN-encapsulated ML MoTe_2 is formed on the PC film, see Fig. S1(e). The hBN/ MoTe_2 /hBN HS is then pressed on the EDC cavity at 110°C . The temperature is then set to 190°C so that

the PC film melts. After 20-30 seconds, the sample is moved away, and the HS remains on the cavity. After that, the sample is cleaned in chloroform for more than 20 minutes and washed with isopropanol (IPA), see Fig. S1(e). The image in Fig. 1(c) in the main text depicts the final result, where Fig. S1(d) and (f) are overlayed with each other for better visibility of the ML MoTe_2 . It is evident from Fig. S1(f) that the sample contains residual polymers from the PC film. As these are likely separated from the MoTe_2 and the EDC cavity by the upper hBN flake, they are not expected to influence the optical properties of the system.

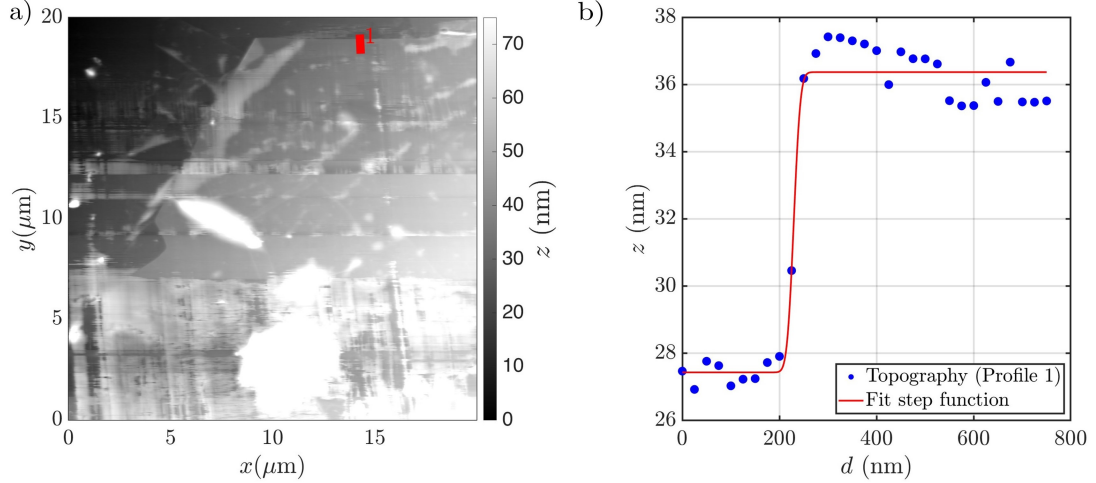


Figure S3. a) AFM map of the final sample, in the region indicated in Fig. S1(f). b) Height profile extracted along line 1 in (a). The red line depicts the fit with an error function.

To confirm the deduced thickness from the optical contrast, an AFM measurement of the final structure is carried out. The AFM map, taken in the region indicated as the dashed rectangle in Fig. S1(f), can be found in Fig. S3(a). Polymer residues are also visible in the AFM measurements. An edge of the upper hBN flake is identified at the top of Fig. S3(a). The extracted height profile along the red line in (a) is depicted in Panel (b). The height profile is fitted with an error function (a convolution of a Gaussian and a step function [101]). This yields $t_{\text{hBN,upper}} = 8.9(6)$ nm, in good agreement with the value obtained with the optical contrast method.

PL spectra at room temperature of the bare EDC cavity before stacking the HS on top, and of the excitonic emission from a monolayer MoTe_2 are compared with the combined system as fabricated, cf. Fig. S4. Clearly, the excitonic emission and the cavity mode can be observed together, demonstrating the successful deposition of the HS on the EDC cavity. It is evident that even without the excitonic emission from MoTe_2 , PL signal from the EDC cavity can be observed. We attribute this to spontaneous recombination in the dielectric material due to the above-bandgap excitation of InP. A Lorentzian fit of the cavity mode emission of the fabricated sample (cf. Fig. S4(c)) reveals a resonance energy of $E_{\text{cav}} = 1.166$ eV and a full-width half-maximum $\Gamma_{\text{cav}} = 3.4$ meV, yielding a quality factor of $Q = 348(7)$ before depositing the hBN/ MoTe_2 /hBN heterostructure on the cavity. It is evident from Fig. S4 that depositing the 2D HS on the EDC cavity blackshifts the resonance energy by ≈ 10 meV, resulting from the increase of the effective refractive index of the cavity mode [75]. Moreover, encapsulating the MoTe_2 flake with hBN and depositing the HS on the EDC cavity blackshifts the excitonic transition by ≈ 6 meV, see Fig. S4, which can be explained by screening of the Coulomb interaction of the electron-hole pairs in the ML TMDC [4, 5, 91]. The cavity linewidth remains unaffected, yielding $\Gamma_{\text{cav}} = 3.3(1)$ meV after depositing the HS on the cavity, corresponding to $Q = 358 \pm 11$.

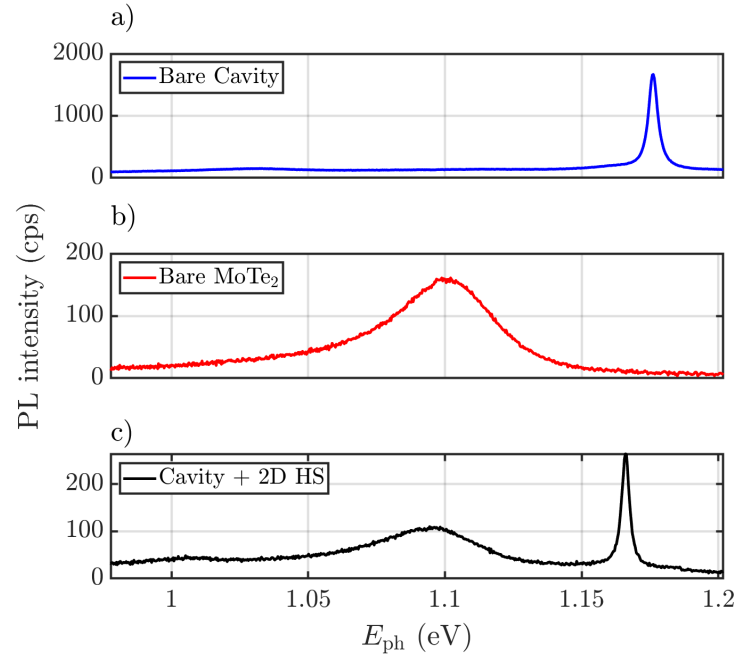


Figure S4. PL spectra at room temperature, of a) the EDC cavity before stacking the hBN/ MoTe_2 /hBN heterostructure on top, of b) a MoTe_2 layer on PDMS and of c) the combined system.

Details on simulations

Subject to suitable radiation conditions [80], the electric-field QNMs $\mathbf{f}_j(\mathbf{r})$ are solutions to the source-less wave equation

$$\nabla \times \nabla \times \tilde{\mathbf{f}}_j(\mathbf{r}) - \tilde{k}_j^2 \epsilon_{\mathbf{R}}(\mathbf{r}) \tilde{\mathbf{f}}_j(\mathbf{r}) = 0 \quad (\text{S1})$$

in which $\epsilon_{\mathbf{R}}(\mathbf{r})$ is the spatially-dependent relative permittivity and the index j labels the different QNMs with corresponding wavenumber $\tilde{k}_j^2 = \tilde{\omega}_j/c$, where $\tilde{\omega}_j$ is the complex eigenfrequency. Even for purely real permittivities, the complex frequencies account for a finite dissipation due to radiation, which means that the field leaks away from the cavity and eventually diverges at large distances. Nevertheless, the QNMs can be normalized by one of several complementary formulas [102]. This also has implications for the expression for the coupling strength in Eq. (1), for which the divergent integral was regularized by use of a quasistatic approximation to the Green tensor in Ref. [59]. For the present calculation, we used a finite area of 2D material and the field was sufficiently localized, that we could ignore this issue and calculate the coupling strength simply by an integral across the extend of the cavity using the normalized field profile $\tilde{\mathbf{F}}_j(\mathbf{r}) = \tilde{\mathbf{f}}_j(\mathbf{r})/\sqrt{\langle\langle\tilde{\mathbf{f}}_j|\tilde{\mathbf{f}}_j\rangle\rangle}$, in which $\sqrt{\langle\langle\tilde{\mathbf{f}}_j|\tilde{\mathbf{f}}_j\rangle\rangle}$ denotes the normalization.

For the eigenmode analysis, we used a finite-element method calculation with the commercial software COMSOL Multiphysics, solving Eq. (S1) numerically following the approach in Ref. [75]. The thicknesses of the hBN layers were determined as described in Sec. . For simplification, the thin ML MoTe₂ (thickness of 0.65 nm [33]) was not included in the calculations. The simulation domain included the structured 245 nm thick InP membrane and an hBN layer with a thickness of 10.5 nm. The integral in Eq. (1) of the main text was evaluated at $z_{2D} = 1.5$ nm above the cavity surface, corresponding to the thickness of the lower hBN flake. The constants a_B and \mathbf{p}_{cv}^α was calculated with values from [33, 88, 89, 103]. The refractive index of hBN and InP was taken from Refs. [90] and [85, 86], respectively.

Fig. S5 depicts the simulated electric field profile. Panel (a) shows $|\tilde{\mathbf{F}}|$ in the plane of the MoTe₂ layer (cf. Fig 1(e) in the main text). Moreover, the field profiles along the Y and X axes are shown in (b) and (c), respectively. A fit with a Gaussian function of the form

$$|\mathbf{F}(x)| = \frac{A}{\sigma\sqrt{2\pi}} e^{-\frac{x^2}{2\sigma^2}} \quad (\text{S2})$$

is indicated by the red lines. Here, x denotes the spatial coordinate (X, Y), and A and σ denote fit parameters. This yields a lateral confinement of $\sigma \approx 70$ nm, much smaller than $\lambda_{\text{cav}}/(2n_{\text{InP}}) = 1049 \text{ nm}/6.4 = 164$ nm.

A convergence study was carried out as described in Ref. [75], yielding $E_{\text{cav}}^{\text{sim}} = 1.18696 \pm 1 \times 10^{-5}$ eV, $\Gamma_{\text{cav}}^{\text{sim}} = 2.07(3)$ meV and $V_{\text{eff}} = (0.060 \pm 0.002)(\lambda/n)^3$.

The thickness of the lower hBN flake has been determined as 1.5(13) nm (see Sec.). The lower hBN flake separates the ML MoTe₂ from the surface of the InP layer via z_{2D} in Eq. 1 in the main text. To assess the uncertainty on the light-matter interaction strength induced by the uncertainty of the thickness of the lower hBN flake (see Sec.), Eq. 1 is evaluated as a function of $t_{\text{hBN,lower}}$. Fig. S6 depicts g_{theory} as a function of the thickness of the lower hBN flake within the uncertainty range of $t_{\text{hBN,lower}}$. At the limiting points of $t_{\text{hBN,lower}} = 0.2$ nm and $t_{\text{hBN,lower}} = 2.8$ nm, g_{theory} does not differ by more than 0.06 meV from the value evaluated at $t_{\text{hBN,lower}} = 1.5$ nm. The total uncertainty for g is determined from the numerical uncertainty, the uncertainty of the material parameters [33, 87–89] and the uncertainty induced by $t_{\text{hBN,lower}}$, yielding $g_{\text{theory}} = 5.2(7)$ meV.

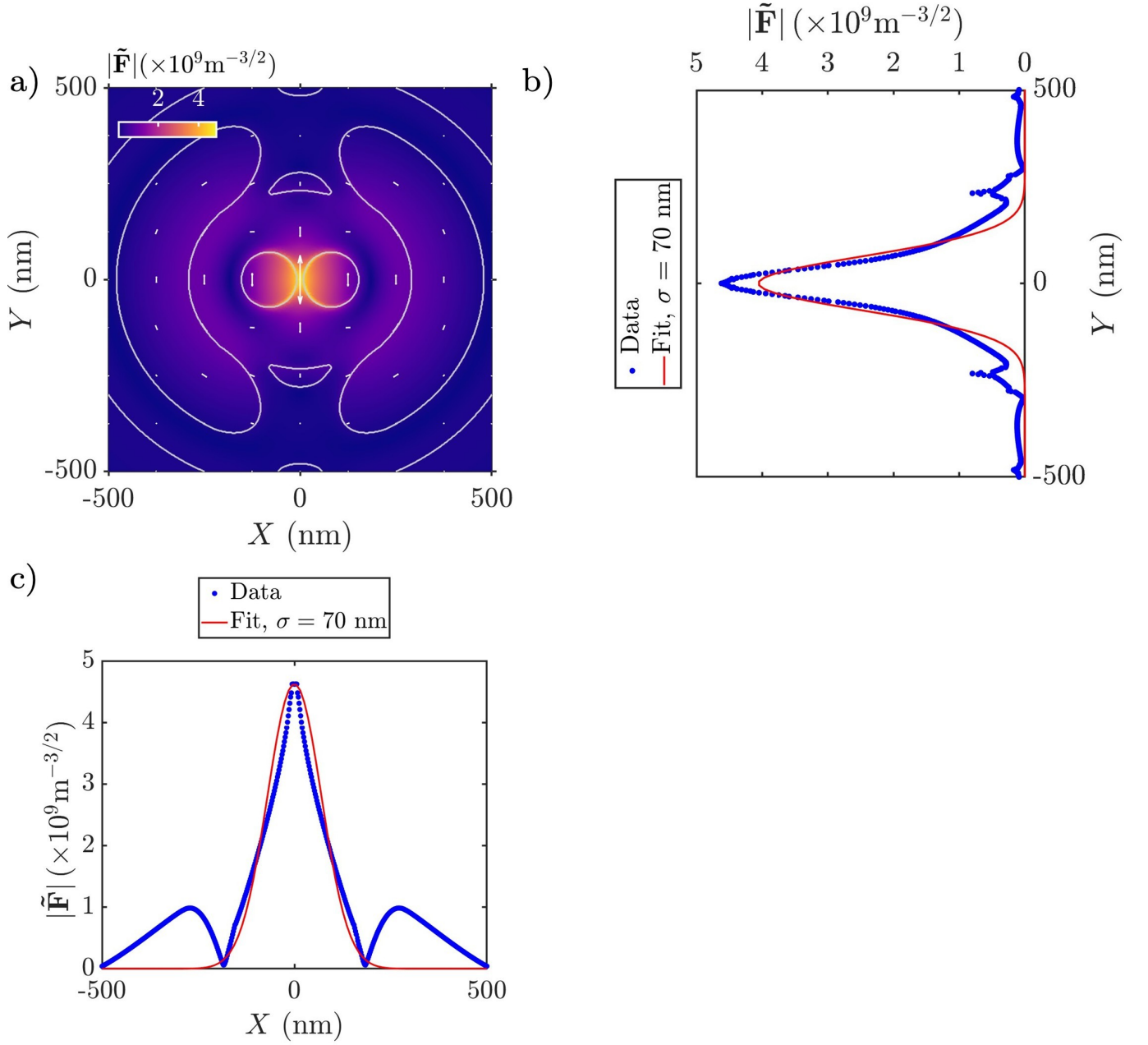


Figure S5. Simulated electric field profile. a) $|\tilde{\mathbf{F}}|$ in the plane of the MoTe_2 layer. The white arrows denote the in-plane polarization. The contour lines show the topography of the cavity at $Z = 0$. Extracted field along the b) Y axis and the c) X axis. A fit with a Gaussian function is indicated as by red lines.

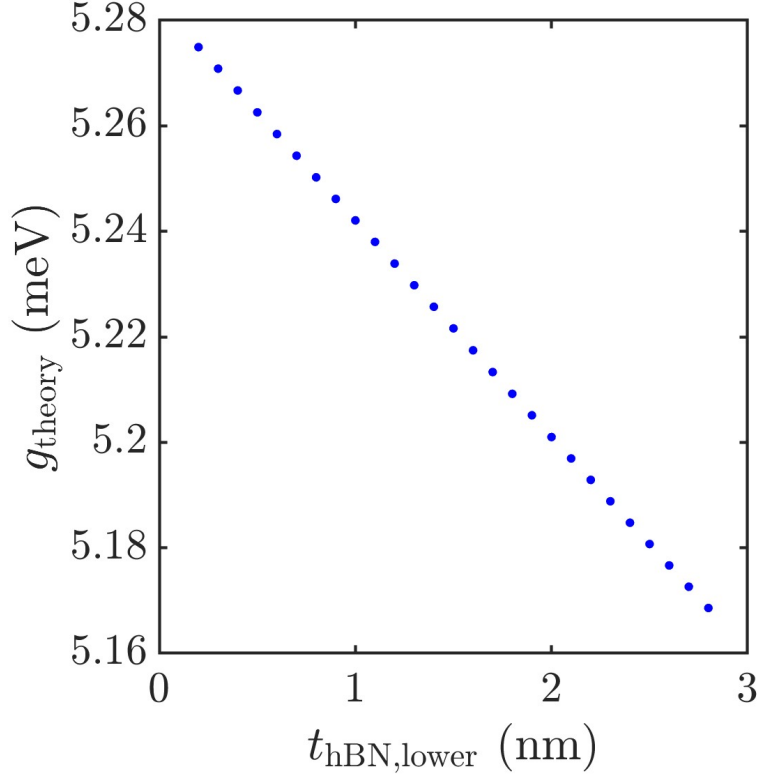


Figure S6. Calculated light-matter interaction strength as a function of the thickness of the lower hBN flake.

Reference measurements

In this Supplementary Information, the reference measurements for deducing $E_{\text{exc}}(T)$, $E_{\text{cav}}(T)$, $\Gamma_{\text{exc}}(T)$ and $\Gamma_{\text{cav}}(T)$ are described.

Fig. S7 depicts spectra as a function of temperatures of a reference cavity. For those measurements, the detection polarization is aligned with the polarization of the cavity mode. Each spectrum is fitted with a single Lorentzian (cf. Fig. S14), yielding $E_{\text{cav,ref}}(T)$ and $\Gamma_{\text{cav,ref}}(T)$ (see Fig. S8), where the subscript "ref" indicates that these values are obtained from a reference cavity. $E_{\text{cav,ref}}(T)$ is fitted with a parabola, $E_{\text{cav,ref}}(T) = y_0 + bT^2$. The obtained temperature dependence of the resonance energy is indicated by the red line in Fig. S7 and Fig. S8(a). Moreover, as evident from Fig. S8(b), the linewidth of the cavity does not depend on temperature as it is not limited by phonon interactions. The deduced offset between $T \leq 70$ K and $T \geq 79$ K due to imperfect alignment of the respective spectrometers used in Setups 1 and 2 is indicated in the inset of Fig. S8 (see Appendix of the main text).

The resonance energy of the reference cavity $E_{\text{cav,ref}}(T)$ deviates from the resonance energy of the cavity with the hBN/MoTe₂/hBN heterostructure $E_{\text{cav}}(T)$ (cf. Fig. S9). This is partially due to the presence of the heterostructure, which changes the effective refractive index of the cavity mode (see Sec.), and partially due to fabrication differences of the cavities, see main text. This overall shift $\Delta = E_{\text{cav,ref}} - E_{\text{cav}}$ is quantified at $T = 293$ K and $T = 315$ K for Setups 1 and Setup 2, respectively, corresponding to a detuning $\delta > 70$ meV. From the coupled-oscillator model it follows that for large detuning, the polaritonic eigenenergies equal the eigenenergies of the respective oscillators. In other words, at this temperature, the influence of the excitonic transition on the cavity mode is negligible. This yields $\Delta = 6.89(3)$ meV and $\Delta = 6.3(1)$ meV for Setup 1 and Setup 2, respectively, see the gray arrow in Fig. S9.

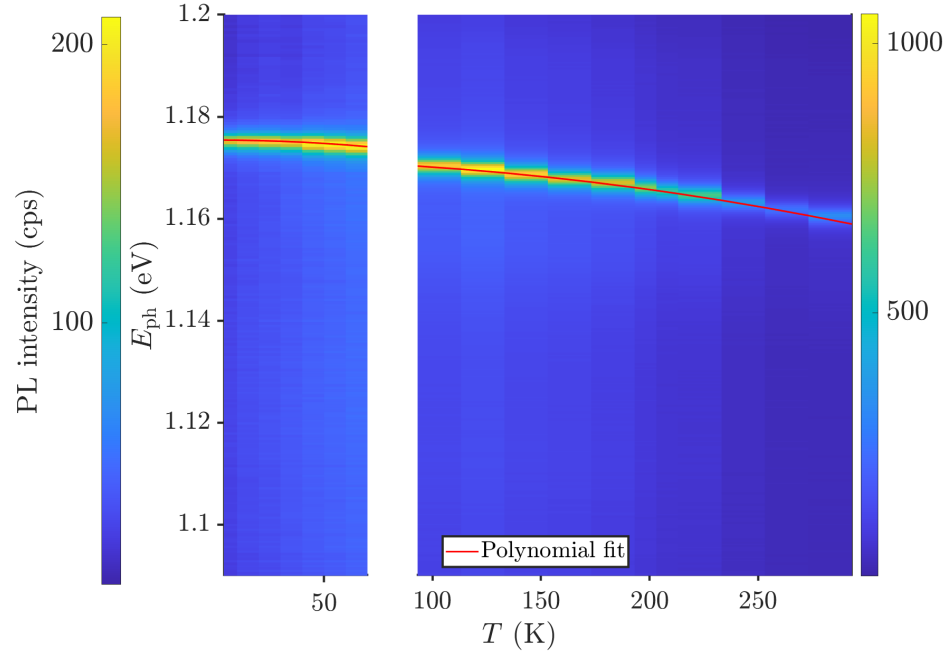


Figure S7. PL spectra as a function of temperature from the reference cavity. The red line indicates a fit of the peak position with a parabola.

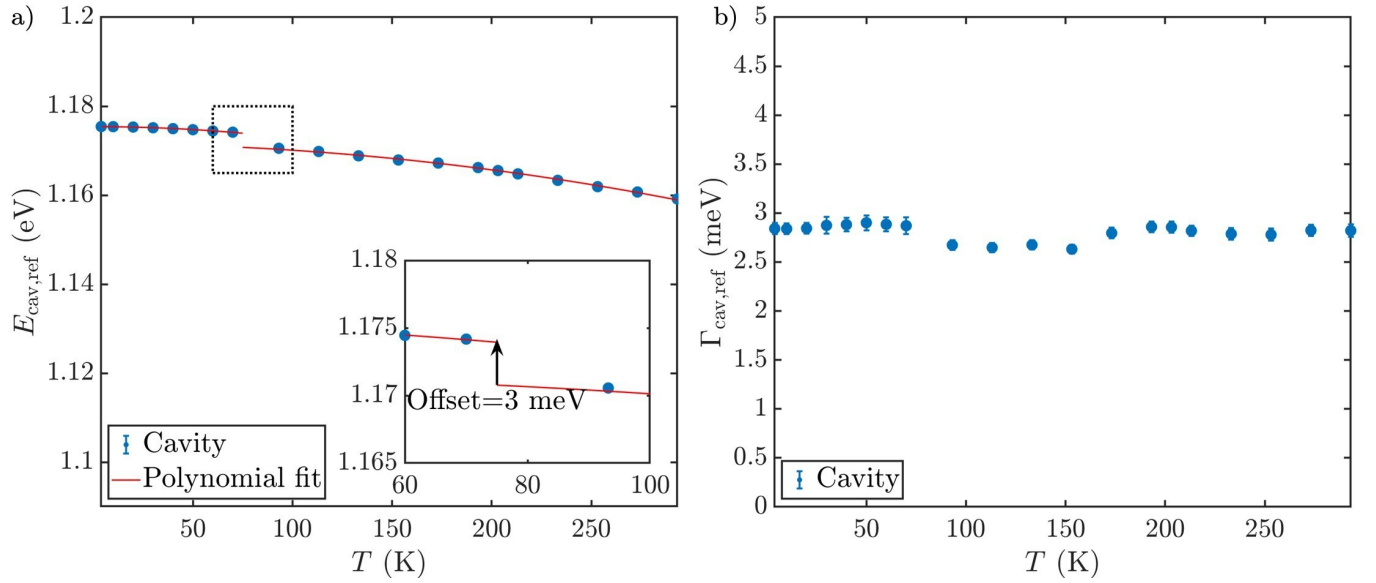


Figure S8. a) Extracted peak positions and b) linewidths of the reference cavity as a function of T . The red line in (a) depicts the fits with a parabola.

The temperature dependence of the cavity can be deduced from the temperature dependence of the reference cavity $E_{\text{cav}}(T) = E_{\text{cav,ref}}(T) + \Delta$. Moreover, since the linewidth of the reference cavity does not depend on the temperature, we use the value for $\Gamma_{\text{cav}} = 3.3(1) \text{ meV}$ deduced from the cavity with the hBN/MoTe₂/hBN heterostructure at

$T = 293$ K (cf. Fig. S9) as the cavity's reference linewidth for all temperatures.

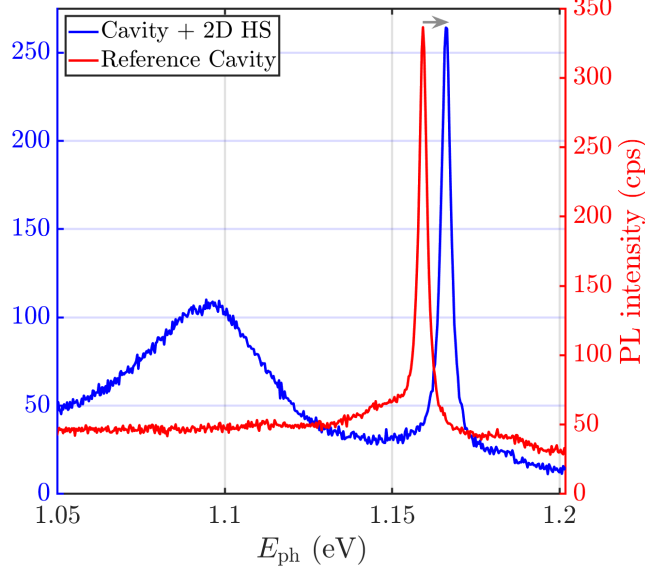


Figure S9. PL spectra at $T = 293$ K for the reference cavity and the sample consisting of EDC cavity and the HS for red and black lines, respectively. The offset Δ is indicated as the grey arrow.

Fig. S10 depicts PL emission spectra of the hBN/MoTe₂/hBN heterostructure on the EDC cavity with the detection polarization perpendicular to the cavity mode. Again, a shift in photon energy is observed between $T \leq 70$ K and $T \geq 79$ K as described above. As described in the main text, this way we obtain emission from uncoupled excitons in the vicinity of the cavity mode. Each spectrum is fitted with two Lorentzian peaks (see also Fig. S13 for a fit at $T = 40$ K). One peak fits the excitonic transition, and the other fits the trion transition stimulating the low- Q mode. This way, the excitonic transition energy $E_{\text{exc}}(T)$ and the linewidth $\Gamma_{\text{exc}}(T)$ are obtained for each temperature, cf. Fig. S11. We observe that signatures of the cavity mode remain faintly visible for higher temperatures, possibly due to non-perfect polarization projection due to scattering from objects in the optical beam path, mainly from the glass window of the cryostat. The low- Q mode [83] is visible throughout the whole measurement series and gets dominant at lower temperatures probably because of excitation by trions [95].

As the temperature dependence of the excitonic transition energy is given by the temperature dependence of the band gap, the extracted $E_{\text{exc}}(T)$ are fitted with the Varshni equation [95]

$$E_{\text{exc}}(T) = E_{\text{exc}}(0) - \frac{\alpha T^2}{T + \beta} \quad (\text{S3})$$

where $E_{\text{exc}}(0)$, α and β are material parameters. The temperature dependence of the exciton is expected to follow previously reported values, so α and β are fixed [95]. This leaves $E_{\text{exc}}(0)$ as the only free fitting parameter. The fit result is indicated as the red line in Fig. S10 and Fig. S11(a), showing good agreement with the obtained PL spectra and deviates by the values found in Ref. [95] by a constant offset. A small but constant offset is likely to occur for different samples and can be explained by a different dielectric environment, yielding differences due to screening of the Coulomb interaction [4]. The data presented in Ref. [95] are measured from a monolayer MoTe₂ on a SiO₂ substrate, whereas our flake is encapsulated in hBN and on a structured InP region (the EDC cavity). This shows that for a quantitative assessment of the reference excitonic energy and, in turn, for the extraction of the light-matter interaction strength, it is highly beneficial to extract the reference from the same sample.

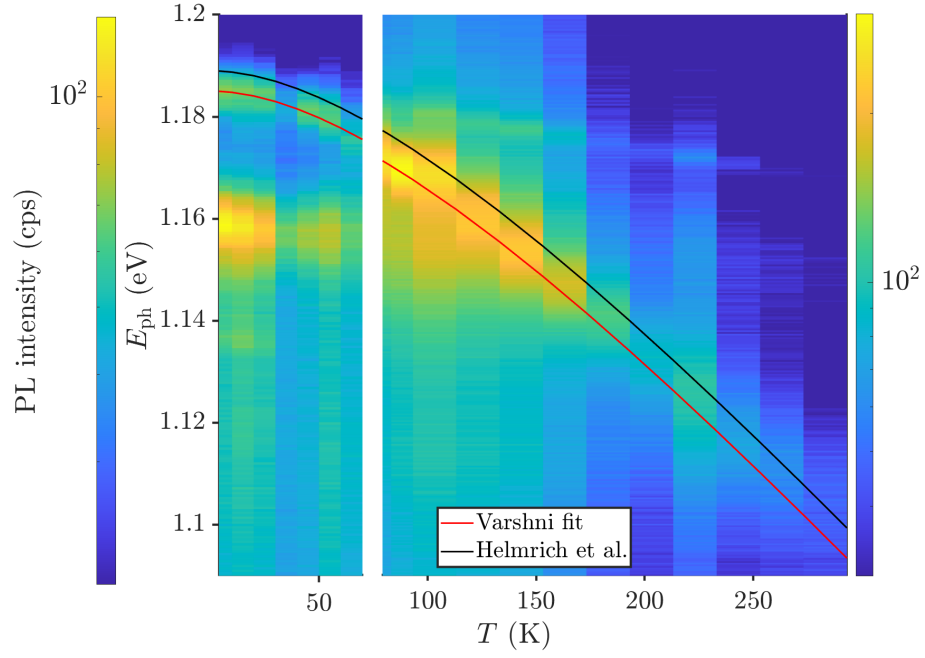


Figure S10. PL spectra as a function of temperature from the hBN/MoTe₂/hBN heterostructure on the EDC cavity with the detection polarization perpendicular to the cavity mode. The red line indicates a Varshni fit of the peak position of the excitonic transition. The black line depicts the temperature dependence of the exciton in MoTe₂ on silicon dioxide found in Ref. [95].

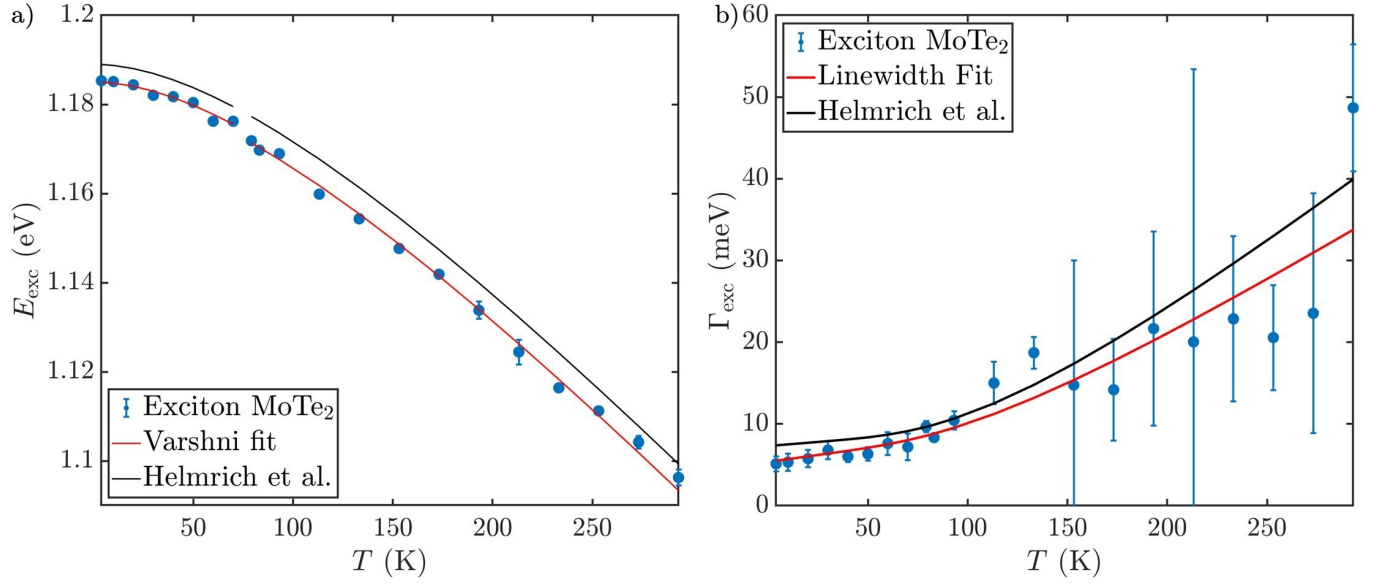


Figure S11. a) Extracted peak positions and b) linewidths of the uncoupled excitons as a function of T . The red lines depict fit results as described in the main text. The black line depicts the temperature dependence of the exciton in MoTe₂ on silicon dioxide found in Ref. [95].

The temperature dependence of the exciton linewidth Γ_{exc} is given as [95]

$$\Gamma_{\text{exc}}(T) = \Gamma_0 + \gamma_{\text{LA}} T + \frac{\Gamma_{\text{LO}}}{\exp(E_{\text{LO}}/k_B T) - 1}, \quad (\text{S4})$$

where Γ_0 denotes the intrinsic linewidth, γ_{LA} the exciton-acoustic phonon strength, and the last term accounts for interaction with longitudinal optical phonons. The extracted linewidth from the spectra in Fig. S10 is depicted in Fig. S11(b). A fit with Eq. S4 is indicated as the red line, and compared to the values obtained in Ref. [95], indicated as the black line. The fit results agree qualitatively, and small deviations are likely to occur due to slightly altered exciton-phonon interaction in different samples. The fit result for Γ_{exc} has a large uncertainty at $T > 150$ K due to the spectral overlap of exciton and trion emission, but gives accurate result close to the region of interest 4 – 140 K where we observe the avoided crossing (see main text). At $T = 4$ K, we extract an exciton linewidth of $\Gamma_{\text{exc}} = 5.1(9)$ meV, in good agreement with the value observed in Ref. [91]. This value is smaller than for ML MoTe₂ on a SiO₂ substrate (around 7 meV [8, 95]), confirming the benefit of hBN encapsulation. While the linewidth is larger than the value reported in [74] (≈ 3 meV for an hBN encapsulated monolayer), a variation on the order of a few meV is often observed for different samples, and explained by local inhomogeneities [91].

The obtained temperature-dependencies for $E_{\text{exc}}(T)$, $E_{\text{cav}}(T)$, $\Gamma_{\text{exc}}(T)$ and $\Gamma_{\text{cav}}(T)$ allow fitting with a coupled-oscillator model with the light-matter interaction strength as the only free fitting parameter. The calculated detuning $\delta(T) = E_{\text{cav}}(T) - E_{\text{exc}}(T)$ is summarized in Tab. II. The uncertainty for T is assumed to be $\sigma_T = \pm 0.5$ K. The uncertainty in the detuning σ_δ is calculated from the uncertainty of E_{exc} , E_{cav} and T with Gaussian error propagation.

$ T \pm 0.5 \text{ (K)} $	$ \delta \text{ (meV)} $	$ \sigma_\delta \text{ (meV)} $
4	-3.3	0.7
10	-3.1	0.7
20	-2.4	0.7
30	-1.5	0.7
40	-0.2	0.7
50	1.3	0.7
60	3.0	0.7
70	4.9	0.7
79	6.2	1.0
83	7.1	1.0
93	9.6	1.0
103	12.1	1.1
113	14.8	1.1
123	17.6	1.1
133	20.4	1.1
143	23.4	1.1
153	26.4	1.1
163	29.5	1.1
173	32.6	1.1
193	39.0	1.1
213	45.5	1.1
233	52.1	1.1
253	58.8	1.1
273	65.6	1.1
293	72.4	1.1

Table II. Measured values for T and corresponding detuning δ and uncertainty σ_δ .

Fits at $T = 40$ K

In this section, we present fits of the spectra of the coupled system and of the references, exemplary at $T = 40$ K, corresponding to $\delta = -0.2(8)$ meV.

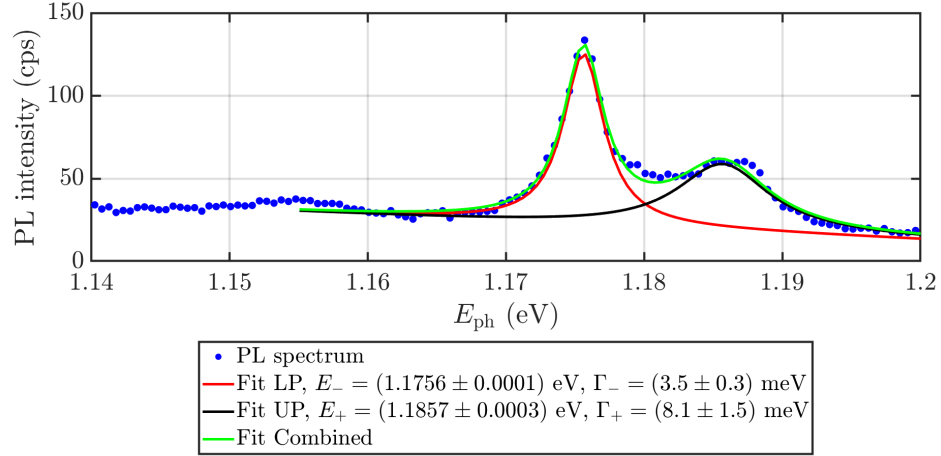


Figure S12. PL spectrum of the hBN/MoTe₂/hBN heterostructure on the EDC cavity at $T = 40$ K with the detection polarization oriented parallel to the cavity mode. Fitting the polaritonic emission is carried out as described in the main text.

Fig. S12 depicts the PL spectrum from the sample consisting of the EDC cavity and the HS with the detection polarization aligned with the polarization of the cavity mode. The lower and upper polariton peaks on a linearly-sloped background are fitted with two Lorentzian lineshapes simultaneously, indicated by the red and black lines in Fig. S12, respectively. The overall fit is indicated as the green line. From the fit, the resonance energies $E_- = 1.176$ eV and $E_+ = 1.186$ eV, as well as the linewidths $\Gamma_- = 3.5(3)$ meV and $\Gamma_+ = 8.1(15)$ meV are obtained.

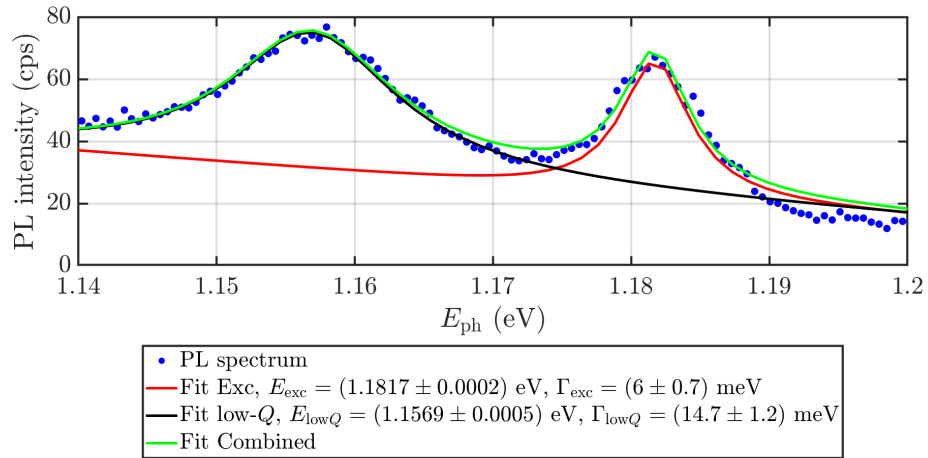


Figure S13. PL spectrum of the hBN/MoTe₂/hBN heterostructure on the EDC cavity at $T = 40$ K with the detection polarization oriented perpendicularly to the cavity mode. Fitting the excitonic emission and the low- Q mode is carried out as described in the main text.

Fig. S13 depicts the PL spectrum from the sample consisting of the EDC cavity and the HS with the detection

polarization perpendicular to the polarization of the cavity mode. The excitonic emission and the low- Q mode are fitted with two Lorentzian peaks on a linearly-sloped background simultaneously, indicated by the red and black lines in Fig. S13, respectively. The fit yields $E_{\text{exc}} = 1.182 \text{ eV}$ and $\Gamma_{\text{exc}} = 6.0(7) \text{ meV}$.

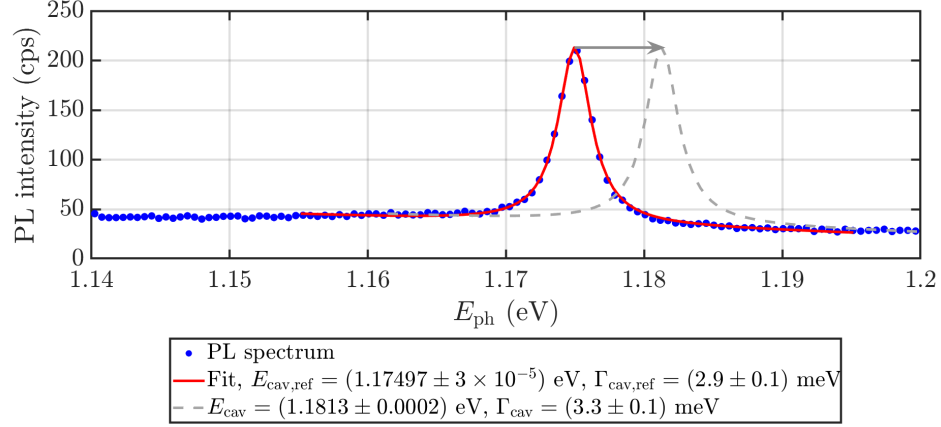


Figure S14. PL spectrum of the reference EDC cavity with the detection polarization parallel to the polarization of the cavity mode. Fitting the cavity mode is carried out as described in the main text. Moreover, the deduced lineshape for E_{cav} and Γ_{cav} (see Sec.), is indicated as the dashed grey line. The length of the grey arrow equals the shift in photon energy Δ , cf. Fig. S9.

Fig. S14 depicts the PL spectrum from the reference EDC cavity with the detection polarization parallel to the polarization of the cavity mode. The emission from the cavity is fitted with a Lorentzian peak on a linearly sloped background, indicated by the red line in Fig. S14. The fit yields $E_{\text{cav,ref}} = 1.175 \text{ eV}$, from which E_{cav} is deduced as 1.181 eV is deduced, see Sec. .

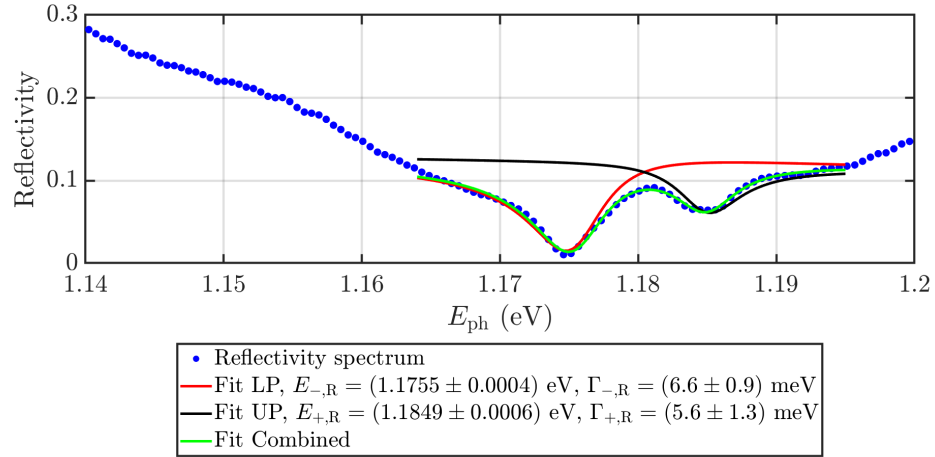


Figure S15. Reflectivity spectrum of the hBN/MoTe2/hBN heterostructure on the EDC cavity at $T = 40 \text{ K}$ in a cross-polarization configuration. Fitting the polaritonic features is carried out as described in the main text.

Fig. S15 depicts the reflectivity spectrum from the sample consisting of the EDC cavity and the HS in a cross-polarization configuration. In reflection measurements, resonances often exhibit Fano lineshapes, resulting from a

superposition of a Lorentzian resonance with a slowly-varying background [83]. Therefore, we fit the reflectivity R in a spectral range close to E_- and E_+ with the equation [22]

$$R(E_{\text{ph}}) = \left| \frac{a_- \Gamma_- / 2 e^{i\varphi_1}}{i(E_{\text{ph}} - E_-) + \Gamma_- / 2} + \frac{a_+ \Gamma_+ / 2 e^{i\varphi_2}}{i(E_{\text{ph}} - E_+) + \Gamma_+ / 2} + \frac{a_{\text{BG}} \Gamma_{\text{BG}} / 2}{i(E_{\text{ph}} - E_{\text{BG}}) + \Gamma_{\text{BG}} / 2} \right|^2. \quad (\text{S5})$$

Here, a_- , a_+ and a_{BG} denote amplitudes for the lower and the upper polaritons and the broad background, respectively, for the chosen polarization settings, and φ_1 and φ_2 take into account potential phase differences between the resonances. From the fit, the resonance energies $E_{-,R} = 1.176$ eV and $E_{+,R} = 1.185$ eV, as well as the linewidths $\Gamma_{-,R} = 6.6(9)$ meV and $\Gamma_{+,R} = 5.6(13)$ meV are found. The subscript "R" indicates that the values are deduced from reflection measurements. These values are in good agreement with the values determined from the PL measurements.

Fit with coupled-oscillator model

The interaction of light and matter can be described by a coupled-oscillator model, where the electromagnetic field in the cavity and the excitonic transition are modeled by two individual harmonic oscillators. The eigenenergies of the coupled states are determined by the eigenvalues of the matrix [9, 84]

$$E_{\pm} = \text{EV} \left(\begin{bmatrix} E_{\text{cav}} - \frac{i\Gamma_{\text{cav}}}{2} & g \\ g & E_{\text{exc}} - \frac{i\Gamma_{\text{exc}}}{2} \end{bmatrix} \right) \quad (\text{S6})$$

Diagonalizing Eq. S6 yields the dispersion relation for the upper (+) and lower (−) polariton

$$E_{\pm} = \frac{1}{2}(E_{\text{cav}} + E_{\text{exc}}) - \frac{i}{4}(\Gamma_{\text{cav}} - \Gamma_{\text{exc}}) \pm \frac{1}{2} \sqrt{4g^2 + \left(\delta - \frac{i}{2}(\Gamma_{\text{cav}} - \Gamma_{\text{exc}}) \right)^2}. \quad (\text{S7})$$

From the dispersion relation in Eq. S7, the Rabi splitting is given by the energy difference at zero detuning

$$E_{\text{Rabi}} = E_+ - E_-|_{\delta=0} = \sqrt{4g^2 - \frac{(\Gamma_{\text{cav}} - \Gamma_{\text{exc}})^2}{4}}. \quad (\text{S8})$$

The system is referred to as strongly coupled if $E_{\text{Rabi}} > (\Gamma_{\text{cav}} + \Gamma_{\text{exc}})/2$, see for example Ref. [11, 104] and references therein.

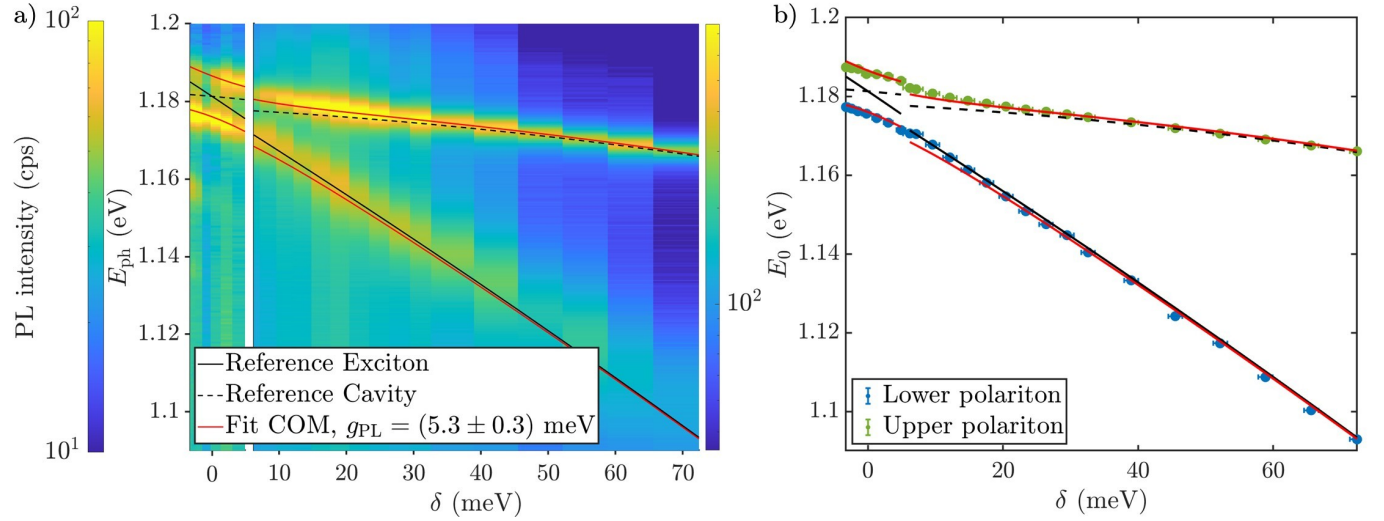


Figure S16. a) PL spectra of the coupled system as a function of detuning over the full temperature range, recorded with the detection polarization aligned with the cavity mode. b) Extracted peak positions from the PL measurements. The solid and dashed black lines depict the reference for the exciton and for the cavity mode, respectively, see Sec. . A fit with the real part of the coupled-oscillator model is indicated by the red lines.

Fig. S16(a) depicts PL spectra shown in Fig. 2 in the main text over the full temperature range, together with fits from reference measurements of the uncoupled cavity and of the uncoupled excitons. As described in Sec. , a shift in photon energy of ≈ 3 meV is observed between $T \leq 70$ K and $T \geq 79$ K, due to imperfect alignment of the respective

spectrometers used in Setups 1 and 2. The extracted peak positions from a Lorentzian fit (cf. Fig. S12) are depicted in Fig. S16(b). Together with the obtained values for E_{cav} , E_{exc} , Γ_{cav} and Γ_{exc} (see Sec.), these are fitted with the real part of the dispersion relation (Eq. S7), leaving g as the only free fitting parameter. The fit of the PL measurements, indicated by the red lines, yields $g_{\text{PL}} = 5.3(3)$ meV.

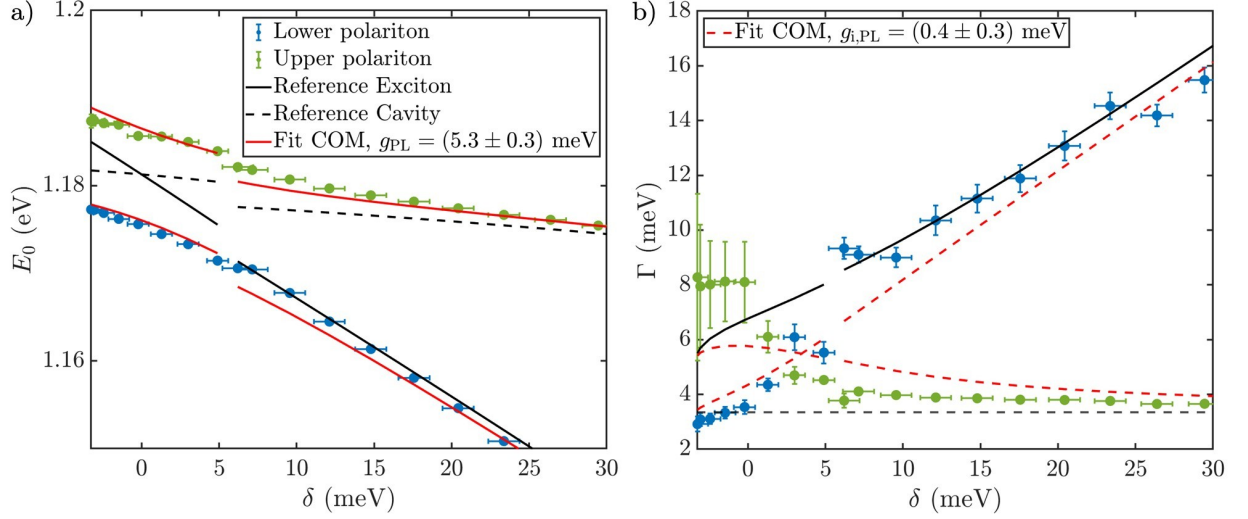


Figure S17. a) Extracted peak positions and b) FWHM of the PL measurements of the coupled system in a region of interest around zero detuning. A fit with the full complex coupled-oscillator model is indicated as solid and dashed red lines for the real and the imaginary parts, respectively.

In general, the light-matter interaction strength is complex $\tilde{g} = g - ig_i$ [51, 94]. To evaluate the magnitude g_i , the complex eigenvalues $\tilde{E}_- = E_- - i\Gamma_-/2$ and $\tilde{E}_+ = E_+ - i\Gamma_+/2$ are fitted with the real and imaginary parts of the dispersion relation (Eq. S7) simultaneously with a complex fit parameter \tilde{g} , exemplary for the PL measurements. Fig. S17(a) depicts the extracted peak positions corresponding to $\text{Re}(\tilde{E}_\pm)$ and (b) shows the extracted linewidth, corresponding to $-2 \text{Im}(\tilde{E}_\pm)$. The fit, indicated as the red solid and dashed lines in (a) and (b), respectively, yields $\tilde{g} = ((5.3 - 0.4i) \pm (0.3 + 0.3i))\text{meV}$. The coupled-oscillator model describes the imaginary part of the spectrum very well, which is additional confirmation of the reported strong light-matter interaction. As the imaginary part of \tilde{g} is less than 6% of the real part and is almost zero within the error bars, it is justified to focus on the real part of the coupled-oscillator model in this case.

Fig. S18(a) depicts reflectivity spectra shown in Fig. 2 in the main text over the full temperature range. The extracted peak positions from a Fano fit (cf. Fig. S15) are depicted in Fig. S18(b). A fit with the real part of the coupled-oscillator model is carried out similarly as for the PL measurements, yielding $g_{\text{R}} = 4.7(7)$ meV. For the reflection measurements, the fit is restricted to $T < 180$ K since the signal-to-noise ratio of the lower polariton becomes small, which is associated with large uncertainties in the fit parameters.

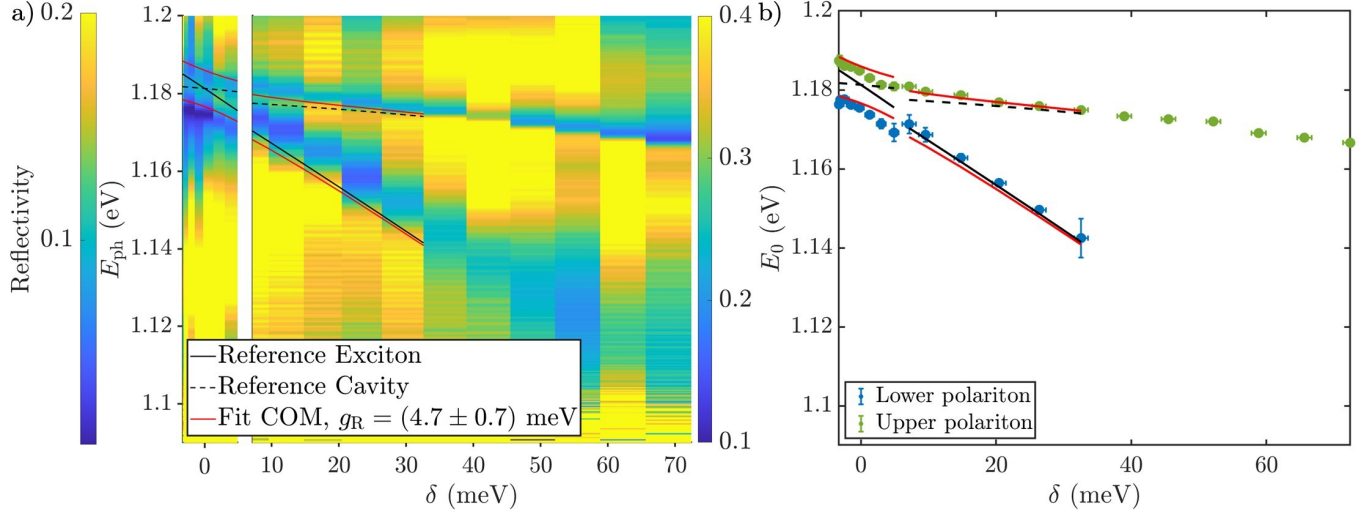


Figure S18. a) Reflectivity spectra of the coupled system as a function of detuning over the full temperature range, recorded with the detection polarization aligned with the cavity mode. b) Extracted peak positions from the reflectivity measurements. The solid and dashed black lines depict the reference for the exciton and for the cavity mode, respectively, see Sec. . A fit with the real part of the coupled-oscillator model is indicated by the red lines.

* Correspondence email address: niste@dtu.dk

- [1] A. Splendiani, L. Sun, Y. Zhang, T. Li, J. Kim, C. Y. Chim, G. Galli, and F. Wang, Emerging photoluminescence in monolayer MoS₂, *Nano Lett.* **10**, 1271 (2010).
- [2] K. F. Mak, C. Lee, J. Hone, J. Shan, and T. F. Heinz, Atomically Thin MoS₂: A New Direct-Gap Semiconductor, *Phys. Rev. Lett.* **105**, 136805 (2010).
- [3] K. He, N. Kumar, L. Zhao, Z. Wang, K. F. Mak, H. Zhao, and J. Shan, Tightly Bound Excitons in Monolayer WSe₂, *Phys. Rev. Lett.* **113**, 026803 (2014).
- [4] A. Chernikov, T. C. Berkelbach, H. M. Hill, A. Rigosi, Y. Li, B. Aslan, D. R. Reichman, M. S. Hybertsen, and T. F. Heinz, Exciton Binding Energy and Nonhydrogenic Rydberg Series in Monolayer WSe₂, *Phys. Rev. Lett.* **113**, 076802 (2014).
- [5] Y. Li, A. Chernikov, X. Zhang, A. Rigosi, H. M. Hill, A. M. van der Zande, D. A. Chenet, E.-M. Shih, J. Hone, and T. F. Heinz, Measurement of the optical dielectric function of monolayer transition-metal dichalcogenides: MoS₂, MoSe₂, WS₂ and WSe₂, *Phys. Rev. B* **90**, 205422 (2014).
- [6] B. Munkhbat, P. Wróbel, T. J. Antosiewicz, and T. O. Shegai, Optical Constants of Several Multilayer Transition Metal Dichalcogenides Measured by Spectroscopic Ellipsometry in the 300–1700 nm Range: High Index, Anisotropy, and Hyperbolicity, *ACS Photonics* **9**, 2398 (2022).
- [7] C. Robert, D. Lagarde, F. Cadiz, G. Wang, B. Lassagne, T. Amand, A. Balocchi, P. Renucci, S. Tongay, B. Urbaszek, and X. Marie, Exciton radiative lifetime in transition metal dichalcogenide monolayers, *Phys. Rev. B* **93**, 1 (2016).
- [8] C. Robert, R. Picard, D. Lagarde, G. Wang, J. P. Echeverry, F. Cadiz, P. Renucci, A. Högele, T. Amand, X. Marie, I. C. Gerber, and B. Urbaszek, Excitonic properties of semiconducting monolayer and bilayer MoTe₂, *Phys. Rev. B* **94**, 155425 (2016).
- [9] C. Schneider, M. M. Glazov, T. Korn, S. Höfling, and B. Urbaszek, Two-dimensional semiconductors in the regime of strong light-matter coupling, *Nat. Commun.* **9**, 2695 (2018).
- [10] P. Törmä and W. L. Barnes, Strong coupling between surface plasmon polaritons and emitters: a review, *Reports Prog. Phys.* **78**, 013901 (2015).
- [11] P. A. Gonçalves, N. Stenger, J. D. Cox, N. A. Mortensen, and S. Xiao, Strong Light–Matter Interactions Enabled by Polaritons in Atomically Thin Materials, *Adv. Opt. Mater.* **8**, 1 (2020).
- [12] C. Tserkezis, A. I. Fernández-Domínguez, P. A. Gonçalves, F. Todisco, J. D. Cox, K. Busch, N. Stenger, S. I. Bozhevolnyi,

- N. A. Mortensen, and C. Wolff, On the applicability of quantum-optical concepts in strong-coupling nanophotonics, *Reports Prog. Phys.* **83**, (2020).
- [13] X. Liu, T. Galfsky, Z. Sun, F. Xia, E.-c. Lin, Y.-H. Lee, S. Kéna-Cohen, and V. M. Menon, Strong light–matter coupling in two-dimensional atomic crystals, *Nat. Photonics* **9**, 30 (2015).
 - [14] S. Dufferwiel, S. Schwarz, F. Withers, A. A. P. Trichet, F. Li, M. Sich, O. Del Pozo-Zamudio, C. Clark, A. Nalitov, D. D. Solnyshkov, G. Malpuech, K. S. Novoselov, J. M. Smith, M. S. Skolnick, D. N. Krizhanovskii, and A. I. Tartakovskii, Exciton–polaritons in van der Waals heterostructures embedded in tunable microcavities, *Nat. Commun.* **6**, 8579 (2015).
 - [15] M. Sidler, P. Back, O. Cotlet, A. Srivastava, T. Fink, M. Kroner, E. Demler, and A. Imamoglu, Fermi polaron-polaritons in charge-tunable atomically thin semiconductors, *Nat. Phys.* **13**, 255 (2017).
 - [16] L. Zhang, R. Gogna, W. Burg, E. Tutuc, and H. Deng, Photonic-crystal exciton-polaritons in monolayer semiconductors, *Nat. Commun.* **9**, 713 (2018).
 - [17] L. Lackner, M. Dusel, O. A. Egorov, B. Han, H. Knopf, F. Eilenberger, S. Schröder, K. Watanabe, T. Taniguchi, S. Tongay, C. Anton-Solanas, S. Höfling, and C. Schneider, Tunable exciton-polaritons emerging from WS₂ monolayer excitons in a photonic lattice at room temperature, *Nat. Commun.* **12**, 4933 (2021).
 - [18] H. Shan, I. Iorsh, B. Han, C. Rupprecht, H. Knopf, F. Eilenberger, M. Esmann, K. Yumigeta, K. Watanabe, T. Taniguchi, S. Klemmt, S. Höfling, S. Tongay, C. Antón-Solanas, I. A. Shelykh, and C. Schneider, Brightening of a dark monolayer semiconductor via strong light-matter coupling in a cavity, *Nat. Commun.* **13**, 3001 (2022).
 - [19] M. Qin, J. Duan, S. Xiao, W. Liu, T. Yu, T. Wang, and Q. Liao, Manipulating strong coupling between exciton and quasibound states in the continuum resonance, *Phys. Rev. B* **105**, 195425 (2022).
 - [20] H. Zheng, Y. Bai, Q. Zhang, and S. Liu, Multi-mode strong coupling in Fabry-Perot cavity-WS₂ photonic crystal hybrid structures, *Opt. Express* **31**, 24976 (2023).
 - [21] E. Maggolini, L. Polimeno, F. Todisco, A. Di Renzo, B. Han, M. De Giorgi, V. Ardizzone, C. Schneider, R. Mastria, A. Cannavale, M. Pugliese, L. De Marco, A. Rizzo, V. Maiorano, G. Gigli, D. Gerace, D. Sanvitto, and D. Ballarini, Strongly enhanced light–matter coupling of monolayer WS₂ from a bound state in the continuum, *Nat. Mater.* **22**, 964 (2023).
 - [22] D. R. Danielsen, N. Lassaline, S. J. Linde, M. V. Nielsen, X. Zambrana-Puyalto, A. Sarbajna, D. H. Nguyen, T. J. Booth, N. Leitherer-Stenger, and S. Raza, Fourier-Tailored Light–Matter Coupling in van der Waals Heterostructures, *ACS Nano* 10.1021/acsnano.5c02025 (2025).
 - [23] L. Sortino, J. Biechteler, L. Lafeta, L. Kühner, A. Hartschuh, L. d. S. Menezes, S. A. Maier, and A. Tittl, Van der Waals heterostructure metasurfaces: atomic-layer assembly of ultrathin optical cavities, *arXiv:2407.16480*.
 - [24] R. B. Iyer, Y. Luan, R. Shinar, J. Shinar, and Z. Fei, Nano-optical imaging of exciton–plasmon polaritons in WSe₂/Au heterostructures, *Nanoscale* **14**, 15663 (2022).
 - [25] L. N. Casses, B. Zhou, Q. Lin, A. Tan, D.-P. Bendixen-Fernex de Mongex, K. J. Kaltenecker, S. Xiao, M. Wubs, and N. Stenger, Full Quantitative Near-Field Characterization of Strongly Coupled Exciton–Plasmon Polaritons in Thin-Layered WSe₂ on a Monocrystalline Gold Platelet, *ACS Photonics* **11**, 3593 (2024).
 - [26] J. Wen, H. Wang, W. Wang, Z. Deng, C. Zhuang, Y. Zhang, F. Liu, J. She, J. Chen, H. Chen, S. Deng, and N. Xu, Room-Temperature Strong Light–Matter Interaction with Active Control in Single Plasmonic Nanorod Coupled with Two-Dimensional Atomic Crystals, *Nano Lett.* **17**, 4689 (2017).
 - [27] M. Stührenberg, B. Munkhbat, D. G. Baranov, J. Cuadra, A. B. Yankovich, T. J. Antosiewicz, E. Olsson, and T. Shegai, Strong Light-Matter Coupling between Plasmons in Individual Gold Bi-pyramids and Excitons in Mono- and Multilayer WSe₂, *Nano Lett.* **18**, 5938 (2018).
 - [28] M. Geisler, X. Cui, J. Wang, T. Rindzevicius, L. Gammelgaard, B. S. Jessen, P. A. D. Gonçalves, F. Todisco, P. Bøggild, A. Boisen, M. Wubs, N. A. Mortensen, S. Xiao, and N. Stenger, Single-Crystalline Gold Nanodisks on WS₂ Mono- and Multilayers for Strong Coupling at Room Temperature, *ACS Photonics* **6**, 994 (2019).
 - [29] B. Munkhbat, D. G. Baranov, A. Bisht, M. A. Hoque, B. Karpiak, S. P. Dash, and T. Shegai, Electrical Control of Hybrid Monolayer Tungsten Disulfide–Plasmonic Nanoantenna Light–Matter States at Cryogenic and Room Temperatures, *ACS Nano* **14**, 1196 (2020).
 - [30] O. Painter, R. K. Lee, A. Scherer, A. Yariv, J. D. O’Brien, P. D. Dapkus, and I. Kim, Two-dimensional photonic band-gap defect mode laser, *Science* **284**, 1819 (1999).
 - [31] Y. Akahane, T. Asano, B. S. Song, and S. Noda, High-Q photonic nanocavity in a two-dimensional photonic crystal, *Nature* **425**, 944 (2003).
 - [32] Y. Ota, R. Katsumi, K. Watanabe, S. Iwamoto, and Y. Arakawa, Topological photonic crystal nanocavity laser, *Commun. Phys.* **1**, 86 (2018).
 - [33] C. Ruppert, B. Aslan, and T. F. Heinz, Optical Properties and Band Gap of Single- and Few-Layer MoTe₂ Crystals, *Nano Lett.* **14**, 6231 (2014).
 - [34] H. Fang, J. Liu, Q. Lin, R. Su, Y. Wei, T. F. Krauss, J. Li, Y. Wang, and X. Wang, Laser-Like Emission from a Sandwiched MoTe₂ Heterostructure on a Silicon Single-Mode Resonator, *Adv. Opt. Mater.* **7**, 5 (2019).

- [35] D. Rosser, D. Gerace, Y. Chen, Y. Liu, J. Whitehead, A. Ryou, L. C. Andreani, and A. Majumdar, Dispersive coupling between MoSe2 and an integrated zero-dimensional nanocavity, *Opt. Mater. Express* **12**, 59 (2022).
- [36] C. Qian, V. Villafa e, P. Soubelet, A. H tger, T. Taniguchi, K. Watanabe, N. P. Wilson, A. V. Stier, A. W. Holleitner, and J. J. Finley, Nonlocal Exciton-Photon Interactions in Hybrid High-Q Beam Nanocavities with Encapsulated MoS2 Monolayers, *Phys. Rev. Lett.* **128**, 237403 (2022).
- [37] J. T. Robinson, C. Manolatou, L. Chen, and M. Lipson, Ultrasmall Mode Volumes in Dielectric Optical Microcavities, *Phys. Rev. Lett.* **95**, 143901 (2005).
- [38] S. Hu and S. M. Weiss, Design of Photonic Crystal Cavities for Extreme Light Concentration, *ACS Photonics* **3**, 1647 (2016).
- [39] H. Choi, M. Heuck, and D. Englund, Self-Similar Nanocavity Design with Ultrasmall Mode Volume for Single-Photon Nonlinearities, *Phys. Rev. Lett.* **118**, 223605 (2017).
- [40] S. Hu, M. Khater, R. Salas-Montiel, E. Kratschmer, S. Engelmann, W. M. Green, and S. M. Weiss, Experimental realization of deep-subwavelength confinement in dielectric optical resonators, *Sci. Adv.* **4**, (2018).
- [41] A. N. Babar, T. A. S. Weis, K. Tsoukalas, S. Kadkhodazadeh, G. Arregui, B. Vosoughi Lahijani, and S. Stobbe, Self-assembled photonic cavities with atomic-scale confinement, *Nature* **624**, 57 (2023).
- [42] M. Albrechtsen, B. Vosoughi Lahijani, R. E. Christiansen, V. T. H. Nguyen, L. N. Casses, S. E. Hansen, N. Stenger, O. Sigmund, H. Jansen, J. M rk, and S. Stobbe, Nanometer-scale photon confinement in topology-optimized dielectric cavities, *Nat. Commun.* **13**, 6281 (2022).
- [43] M. Xiong, R. E. Christiansen, F. Schr der, Y. Yu, L. N. Casses, E. Semenova, K. Yvind, N. Stenger, O. Sigmund, and J. M rk, Experimental realization of deep sub-wavelength confinement of light in a topology-optimized InP nanocavity, *Opt. Mater. Express* **14**, 397 (2024).
- [44] J. S. Jensen and O. Sigmund, Topology optimization for nano-photonics, *Laser Photonics Rev.* **5**, 308 (2011).
- [45] S. Molesky, Z. Lin, A. Y. Piggott, W. Jin, J. Vuckovi , and A. W. Rodriguez, Inverse design in nanophotonics, *Nat. Photonics* **12**, 659 (2018).
- [46] F. Wang, R. E. Christiansen, Y. Yu, J. M rk, and O. Sigmund, Maximizing the quality factor to mode volume ratio for ultra-small photonic crystal cavities, *Appl. Phys. Lett.* **113**, (2018).
- [47] F. Wang and Y. R. Shen, General properties of local plasmons in metal nanostructures, *Phys. Rev. Lett.* **97**, 1 (2006).
- [48] G. V. Naik, V. M. Shalaev, and A. Boltasseva, Alternative plasmonic materials: Beyond gold and silver, *Adv. Mater.* **25**, 3264 (2013).
- [49] J. B. Khurgin, How to deal with the loss in plasmonics and metamaterials, *Nat. Nanotechnol.* **10**, 2 (2015).
- [50] M. V. Gurrieri, E. V. Denning, K. Seegert, P. T. Kristensen, and J. M rk, Dynamics and condensation of polaritons in an optical nanocavity coupled to two-dimensional materials, *Phys. Rev. B* **109**, 1 (2024).
- [51] M. Abutoama, G. Kountouris, J. M rk, and P. T. Kristensen, Modal approach to the coupling strength of quantum emitters in electromagnetic resonators, *Phys. Rev. B* **110**, 195434 (2024).
- [52] G. Dong, A. N. Babar, R. E. Christiansen, S. E. Hansen, S. Stobbe, Y. Yu, and J. M rk, Enhancement and speed-up of carrier dynamics in a dielectric nanocavity with deep sub-wavelength confinement, *arXiv:2412.08471*.
- [53] G. Kountouris, A. S. Darket, L. Vestergaard, E. V. Denning, J. M rk, and P. T. Kristensen, Lithographically defined quantum dot with subwavelength confinement of light, *Phys. Rev. B* **110**, L241301 (2024).
- [54] M. Xiong, Y. Yu, Y. Berdnikov, S. K. Borregaard, A. H. Dubr , E. Semenova, K. Yvind, and J. M rk, A nanolaser with extreme dielectric confinement, *arXiv:2412.02844*.
- [55] K. Momma and F. Izumi, VESTA 3 for three-dimensional visualization of crystal, volumetric and morphology data, *J. Appl. Crystallogr.* **44**, 1272 (2011).
- [56] A. Jain, S. P. Ong, G. Hautier, W. Chen, W. D. Richards, S. Dacek, S. Cholia, D. Gunter, D. Skinner, G. Ceder, and K. A. Persson, Commentary: The Materials Project: A materials genome approach to accelerating materials innovation, *APL Mater.* **1**, (2013).
- [57] B. Besga, C. Vanep, J. Reichel, J. Est ve, A. Reinhard, J. Miguel-S nchez, A. Imamog lu, and T. Volz, Polariton Boxes in a Tunable Fiber Cavity, *Phys. Rev. Appl.* **3**, 014008 (2015).
- [58] G. Mu oz-Matutano, A. Wood, M. Johnsson, X. Vidal, B. Q. Baragiola, A. Reinhard, A. Lema tre, J. Bloch, A. Amo, G. Nogues, B. Besga, M. Richard, and T. Volz, Emergence of quantum correlations from interacting fibre-cavity polaritons, *Nat. Mater.* **18**, 213 (2019).
- [59] E. V. Denning, M. Wubs, N. Stenger, J. M rk, and P. T. Kristensen, Quantum theory of two-dimensional materials coupled to electromagnetic resonators, *Phys. Rev. B* **105**, 85306 (2022).
- [60] M. Bamba, A. Imamog lu, I. Carusotto, and C. Ciuti, Origin of strong photon antibunching in weakly nonlinear photonic molecules, *Phys. Rev. A* **83**, 21802 (2011).
- [61] A. Ryou, D. Rosser, A. Saxena, T. Fryett, and A. Majumdar, Strong photon antibunching in weakly nonlinear two-dimensional exciton-polaritons, *Phys. Rev. B* **97**, 235307 (2018).
- [62] E. V. Denning, M. Wubs, N. Stenger, J. M rk, and P. T. Kristensen, Cavity-induced exciton localization and polariton

- blockade in two-dimensional semiconductors coupled to an electromagnetic resonator, *Phys. Rev. Res.* **4**, L012020 (2022).
- [63] O. Kyriienko, D. N. Krizhanovskii, and I. A. Shelykh, Nonlinear Quantum Optics with Trion Polaritons in 2D Monolayers: Conventional and Unconventional Photon Blockade, *Phys. Rev. Lett.* **125**, 197402 (2020).
 - [64] A. Delteil, T. Fink, A. Schade, S. Höfling, C. Schneider, and A. İmamoğlu, Towards polariton blockade of confined exciton–polaritons, *Nat. Mater.* **18**, 219 (2019).
 - [65] D. Xiao, G. B. Liu, W. Feng, X. Xu, and W. Yao, Coupled spin and valley physics in monolayers of MoS₂ and other group-VI dichalcogenides, *Phys. Rev. Lett.* **108**, 1 (2012).
 - [66] K. F. Mak, K. He, J. Shan, and T. F. Heinz, Control of valley polarization in monolayer MoS₂ by optical helicity, *Nat. Nanotechnol.* **7**, 494 (2012).
 - [67] L. Yang, N. A. Sinitsyn, W. Chen, J. Yuan, J. Zhang, J. Lou, and S. A. Crooker, Long-lived nanosecond spin relaxation and spin coherence of electrons in monolayer MoS₂ and WS₂, *Nat. Phys.* **11**, 830 (2015).
 - [68] C. F. Fong, Y. Ota, Y. Arakawa, S. Iwamoto, and Y. K. Kato, Chiral modes near exceptional points in symmetry broken H1 photonic crystal cavities, *Phys. Rev. Res.* **3**, 043096 (2021).
 - [69] P. Cheben, R. Halir, J. H. Schmid, H. A. Atwater, and D. R. Smith, Subwavelength integrated photonics, *Nature* **560**, 565 (2018).
 - [70] J. Wang, F. Sciarrino, A. Laing, and M. G. Thompson, Integrated photonic quantum technologies, *Nat. Photonics* **14**, 273 (2020).
 - [71] B. Chen, H. Sahin, A. Suslu, L. Ding, M. I. Bertoni, F. M. Peeters, and S. Tongay, Environmental Changes in MoTe₂ Excitonic Dynamics by Defects-Activated Molecular Interaction, *ACS Nano* **9**, 5326 (2015).
 - [72] O. A. Ajayi, J. V. Ardelean, G. D. Shepard, J. Wang, A. Antony, T. Taniguchi, K. Watanabe, T. F. Heinz, S. Strauf, X. Y. Zhu, and J. C. Hone, Approaching the intrinsic photoluminescence linewidth in transition metal dichalcogenide monolayers, *2D Mater.* **4**, (2017).
 - [73] F. Cadiz, E. Courtade, C. Robert, G. Wang, Y. Shen, H. Cai, T. Taniguchi, K. Watanabe, H. Carrere, D. Lagarde, M. Manca, T. Amand, P. Renucci, S. Tongay, X. Marie, and B. Urbaszek, Excitonic Linewidth Approaching the Homogeneous Limit in MoS₂-Based van der Waals Heterostructures, *Phys. Rev. X* **7**, 021026 (2017).
 - [74] B. Han, C. Robert, E. Courtade, M. Manca, S. Shree, T. Amand, P. Renucci, T. Taniguchi, K. Watanabe, X. Marie, L. E. Golub, M. M. Glazov, and B. Urbaszek, Exciton States in Monolayer MoSe₂ and MoTe₂ Probed by Upconversion Spectroscopy, *Phys. Rev. X* **8**, 1 (2018).
 - [75] G. Kountouris, J. Mørk, E. V. Denning, and P. T. Kristensen, Modal properties of dielectric bowtie cavities with deep sub-wavelength confinement, *Opt. Express* **30**, 40367 (2022).
 - [76] E. S. C. Ching, P. T. Leung, A. Maassen van den Brink, W. M. Suen, S. S. Tong, and K. Young, Quasinormal-mode expansion for waves in open systems, *Rev. Mod. Phys.* **70**, 1545 (1998).
 - [77] E. A. Muljarov, W. Langbein, and R. Zimmermann, Brillouin-Wigner perturbation theory in open electromagnetic systems, *EPL (Europhysics Lett.)* **92**, 50010 (2010).
 - [78] P. T. Kristensen and S. Hughes, Modes and Mode Volumes of Leaky Optical Cavities and Plasmonic Nanoresonators, *ACS Photonics* **1**, 2 (2013).
 - [79] P. Lalanne, W. Yan, K. Vynck, C. Sauvan, and J. Hugonin, Light Interaction with Photonic and Plasmonic Resonances, *Laser Photon. Rev.* **12**, 1 (2018).
 - [80] P. T. Kristensen, K. Herrmann, F. Intravaia, and K. Busch, Modeling electromagnetic resonators using quasinormal modes, *Adv. Opt. Photonics* **12**, 612 (2020).
 - [81] S. Both and T. Weiss, Resonant states and their role in nanophotonics, *Semicond. Sci. Technol.* **37**, 013002 (2021).
 - [82] E. Dimopoulos, A. Sakanas, A. Marchevsky, M. Xiong, Y. Yu, E. Semenova, J. Mørk, and K. Yvind, Electrically-Driven Photonic Crystal Lasers with Ultra-low Threshold, *Laser Photon. Rev.* **16**, 1 (2022).
 - [83] F. Schröder, M. P. van Exter, M. Xiong, G. Kountouris, M. Wubs, P. T. Kristensen, and N. Stenger, Confocal polarization tomography of dielectric nanocavities, *Nanophotonics* 10.1515/nanoph-2024-0744 (2025).
 - [84] C. Carlson, R. Salzwedel, M. Selig, A. Knorr, and S. Hughes, Strong coupling regime and hybrid quasinormal modes from a single plasmonic resonator coupled to a transition metal dichalcogenide monolayer, *Phys. Rev. B* **104**, 125424 (2021).
 - [85] G. D. Pettit and W. J. Turner, Refractive Index of InP, *J. Appl. Phys.* **36**, 2081 (1965).
 - [86] J. A. McCaulley, V. M. Donnelly, M. Vernon, and I. Taha, Temperature dependence of the near-infrared refractive index of silicon, gallium arsenide, and indium phosphide, *Phys. Rev. B* **49**, 7408 (1994).
 - [87] I. C. Gerber and X. Marie, Dependence of band structure and exciton properties of encapsulated WSe₂ monolayers on the hBN-layer thickness, *Phys. Rev. B* **98**, 245126 (2018).
 - [88] L. Meckbach, J. Hader, U. Huttner, J. Neuhaus, J. T. Steiner, T. Stroucken, J. V. Moloney, and S. W. Koch, Ultrafast band-gap renormalization and build-up of optical gain in monolayer MoTe₂, *Phys. Rev. B* **101**, 1 (2020).
 - [89] S. Edalati-Boostan, C. Cocchi, and C. Draxl, MoTe₂ as a natural hyperbolic material across the visible and the ultraviolet region, *Phys. Rev. Mater.* **4**, 1 (2020).
 - [90] D. V. Grudinin, G. A. Ermolaev, D. G. Baranov, A. N. Toksumakov, K. V. Voronin, A. S. Slavich, A. A. Vyshnevyy,

- A. B. Mazitov, I. A. Kruglov, D. A. Ghazaryan, A. V. Arsenin, K. S. Novoselov, and V. S. Volkov, Hexagonal boron nitride nanophotonics: a record-breaking material for the ultraviolet and visible spectral ranges, *Mater. Horizons* **10**, 2427 (2023).
- [91] J. Kutrowska-Girzycka, E. Zieba-Ostój, D. Biegańska, M. Florian, A. Steinhoff, E. Rogowicz, P. Mrowiński, K. Watanabe, T. Taniguchi, C. Gies, S. Tongay, C. Schneider, and M. Syperek, Exploring the effect of dielectric screening on neutral and charged-exciton properties in monolayer and bilayer MoTe₂, *Appl. Phys. Rev.* **9**, 041410 (2022).
 - [92] L. C. Andreani, G. Panzarini, and J.-M. Gérard, Strong-coupling regime for quantum boxes in pillar microcavities: Theory, *Phys. Rev. B* **60**, 13276 (1999).
 - [93] F. Todisco, R. Malureanu, C. Wolff, P. A. D. Gonçalves, A. S. Roberts, N. A. Mortensen, and C. Tserkezis, Magnetic and electric Mie-exciton polaritons in silicon nanodisks, *Nanophotonics* **9**, 803 (2020).
 - [94] O. Bleu, K. Choo, J. Levinsen, and M. M. Parish, Dissipative light-matter coupling and anomalous dispersion in nonideal cavities, *Phys. Rev. A* **109**, 1 (2024).
 - [95] S. Helmrich, R. Schneider, A. W. Achtstein, A. Arora, B. Herzog, S. M. de Vasconcellos, M. Kolarczik, O. Schöps, R. Bratschitsch, U. Woggon, and N. Owschmikow, Exciton-phonon coupling in mono- and bilayer MoTe₂, *2D Mater.* **5**, 45007 (2018).
 - [96] R. V. Gorbachev, I. Riaz, R. R. Nair, R. Jalil, L. Britnell, B. D. Belle, E. W. Hill, K. S. Novoselov, K. Watanabe, T. Taniguchi, A. K. Geim, and P. Blake, Hunting for Monolayer Boron Nitride: Optical and Raman Signatures, *Small* **7**, 465 (2011).
 - [97] P. Holm, *Atomically precise patterning by thermal scanning probe lithography*, Master's thesis, Technical University of Denmark (2024).
 - [98] A. Castellanos-Gomez, M. Buscema, R. Molenaar, V. Singh, L. Janssen, H. S. Van Der Zant, and G. A. Steele, Deterministic transfer of two-dimensional materials by all-dry viscoelastic stamping, *2D Mater.* **1**, 10.1088/2053-1583/1/1/011002 (2014).
 - [99] P. J. Zomer, M. H. Guimarães, J. C. Brant, N. Tombros, and B. J. Van Wees, Fast pick up technique for high quality heterostructures of bilayer graphene and hexagonal boron nitride, *Appl. Phys. Lett.* **105**, 10.1063/1.4886096 (2014).
 - [100] F. Pizzocchero, L. Gammelgaard, B. S. Jessen, J. M. Caridad, L. Wang, J. Hone, P. Bøggild, and T. J. Booth, The hot pick-up technique for batch assembly of van der Waals heterostructures, *Nat. Commun.* **7**, 10.1038/ncomms11894 (2016).
 - [101] L. C. Andrews, *Special Functions of Mathematics for Engineers*, 2nd ed. (SPIE—The International Society for Optical Engineering and Oxford University Press, 1997).
 - [102] P. T. Kristensen, R.-C. Ge, and S. Hughes, Normalization of quasinormal modes in leaky optical cavities and plasmonic resonators, *Phys. Rev. A* **92**, 053810 (2015).
 - [103] S. Hastrup, M. Strange, M. Pandey, T. Deilmann, P. S. Schmidt, N. F. Hinsche, M. N. Gjerding, D. Torelli, P. M. Larsen, A. C. Riis-Jensen, J. Gath, K. W. Jacobsen, J. Jørgen Mortensen, T. Olsen, and K. S. Thygesen, The Computational 2D Materials Database: high-throughput modeling and discovery of atomically thin crystals, *2D Mater.* **5**, 042002 (2018).
 - [104] F. Hu and Z. Fei, Recent Progress on Exciton Polaritons in Layered Transition-Metal Dichalcogenides, *Adv. Opt. Mater.* **8**, 1 (2020).